


Large-eddy simulation of nitrogen injection at trans- and supercritical conditions

Cite as: Phys. Fluids **28**, 015102 (2016); <https://doi.org/10.1063/1.4937948>

Submitted: 12 March 2015 . Accepted: 01 December 2015 . Published Online: 06 January 2016

Hagen Müller , Christoph A. Niedermeier, Jan Matheis, Michael Pfitzner, and Stefan Hickel 



View Online



Export Citation



CrossMark

ARTICLES YOU MAY BE INTERESTED IN

[A numerical study of cryogenic fluid injection and mixing under supercritical conditions](#)

Physics of Fluids **16**, 4248 (2004); <https://doi.org/10.1063/1.1795011>

[Experiments and numerical simulation of mixing under supercritical conditions](#)

Physics of Fluids **24**, 055104 (2012); <https://doi.org/10.1063/1.3701374>

[The absence of a dense potential core in supercritical injection: A thermal break-up mechanism](#)

Physics of Fluids **28**, 035103 (2016); <https://doi.org/10.1063/1.4943038>

 Highlights of the best new research
in the **physical sciences**
[LEARN MORE!](#)





Large-eddy simulation of nitrogen injection at trans- and supercritical conditions

Hagen Müller,¹ Christoph A. Niedermeier,² Jan Matheis,² Michael Pfitzner,¹ and Stefan Hickel^{2,3,a)}

¹*Institute of Thermodynamics, Universität der Bundeswehr München, Werner-Heisenberg-Weg 39, 85577 Neubiberg, Germany*

²*Institute of Aerodynamics and Fluid Mechanics, Technische Universität München, Boltzmannstr. 15, 85748 Garching b. München, Germany*

³*Faculty of Aerospace Engineering, Technische Universiteit Delft, Kluyverweg 1, 2629 HS Delft, The Netherlands*

(Received 12 March 2015; accepted 1 December 2015; published online 6 January 2016)

Large-eddy simulations (LESs) of cryogenic nitrogen injection into a warm environment at supercritical pressure are performed and real-gas thermodynamics models and subgrid-scale (SGS) turbulence models are evaluated. The comparison of different SGS models — the Smagorinsky model, the Vreman model, and the adaptive local deconvolution method — shows that the representation of turbulence on the resolved scales has a notable effect on the location of jet break-up, whereas the particular modeling of unresolved scales is less important for the overall mean flow field evolution. More important are the models for the fluid's thermodynamic state. The injected fluid is either in a supercritical or in a transcritical state and undergoes a pseudo-boiling process during mixing. Such flows typically exhibit strong density gradients that delay the instability growth and can lead to a redistribution of turbulence kinetic energy from the radial to the axial flow direction. We evaluate novel volume-translation methods on the basis of the cubic Peng-Robinson equation of state in the framework of LES. At small extra computational cost, their application considerably improves the simulation results compared to the standard formulation. Furthermore, we found that the choice of inflow temperature is crucial for the reproduction of the experimental results and that heat addition within the injector can affect the mean flow field in comparison to results with an adiabatic injector. © 2016 AIP Publishing LLC. [<http://dx.doi.org/10.1063/1.4937948>]

I. INTRODUCTION

Many energy conversion devices, such as liquid rocket engines (LREs), operate at pressures that exceed the critical pressure of the involved fluids. The operating pressure of gas-expander-cycle LREs lies typically above 10 MPa and is thus higher than the critical pressure p_c of common propellants like oxygen ($p_{c,O_2} = 5.0$ MPa) or hydrogen ($p_{c,H_2} = 1.3$ MPa). The main argument for high operating pressures is the proportionality between operating pressure and specific impulse of the LRE.¹ The same trend can be observed in aircraft or automotive engines where the need for reducing CO₂ and NO_x emissions motivates the increase of the pressure. A further important characteristics of most main stage LREs is the cryogenic temperature, with which one or both propellants enter the thrust chamber. In the Vulcain 2 engine for instance, the injection temperature of oxygen is approximately 96.7 K and thus well below its pseudo-boiling temperature, which represents the prolongation of the saturated-vapor and saturated-liquid curve. The injected propellant is then in a *transcritical state*, often referred to as a *compressed* or *dense* gas. Compressed gases have a high liquid-like density and viscosity. The crucial difference to liquids is that the molecular

^{a)}Electronic mail: S.Hickel@tudelft.nl

repulsive forces are strong enough to overcome the surface tension. As a consequence, transcritical jet disintegration differs significantly from injection at lower pressures, where droplet formation, evaporation, and subsequent ignition are the controlling phenomena. The transcritical process is rather characterized by the formation of finger-like structures of dense fluid that emerge from the jet core and mix quickly with the surrounding fluid.²

The biggest steps towards a better understanding of cryogenic propellant injection in high-pressure environments were made in the last 20 years³ when numerous experimental studies have led to a clearer picture of the governing mechanisms and computational fluid dynamics (CFD) approached a predictive quality. Much experimental work was done on cryogenic nitrogen injection into a supercritical nitrogen atmosphere.^{4–8} These fundamental studies emphasize the strong influence of the thermodynamic state on the jet development. **It was, for instance, observed that increasing the injection temperature by 10 K and thereby crossing the pseudo-boiling temperature significantly reduces the length of the potential core.** This sensitive behavior is mainly attributed to the strong density-temperature coupling and the high heat capacities in the vicinity of the pseudo-critical temperature. Along with experimental studies, many groups investigated this configuration numerically. Numerical simulations are highly challenging, since the typical conditions are characterized by regions of high density gradients as well as by highly non-linear dependencies between transport properties, caloric properties, and thermodynamic state variables. The demands on modeling accuracy, discretization, and numerical robustness are high and need to be addressed carefully on the way towards predictive simulations. The Raman density measurements of Mayer *et al.*,⁴ for example, allow hereby for a quantitative assessment of the models' ability to describe the thermodynamic effects associated with surpassing the pseudo-boiling temperature.

Pioneering work in the context of large-eddy simulation (LES) was reported by Oefelein and Yang⁹ and later by Zong *et al.*^{10,11} as well as by Oefelein,¹² who implemented detailed real-gas thermodynamics and transport models into their density-based flow solvers. **Zong *et al.*¹¹ show that the high density gradient between injected and surrounding fluid effectively damps the velocity fluctuations normal to the jet surface and amplifies fluctuations in axial direction.** The growth rate of the Kelvin-Helmholtz instability leading to vortex formation and finally to jet break-up is thus slowed down. Schmitt *et al.*¹³ performed LES using the cubic Peng-Robinson (PR)¹⁴ equation of state (EoS). **Their results are in good quantitative agreement with the experimental data of Mayer *et al.*,⁴ for transcritical injection.** Later, Kim *et al.*¹⁵ compared two cubic EoSs, the PR EoS and the Soave-Redlich-Kwong (SRK)¹⁶ EoS, in the context of the Reynolds averaged Navier-Stokes (RANS) equations, showing that the choice of an EoS has a significant influence, not only on the thermodynamic state variables but also on the turbulence intensities. However, both EoSs exhibit non-negligible inaccuracies in the transcritical region. For the testing conditions of the experiments of Mayer *et al.*,⁴ for instance, the density deviates by up to 12.3% from the NIST chemistry web-book¹⁷ reference data. Urbano and Nasuti¹⁸ therefore implemented the GERG EoS,¹⁹ which is based on modeling the Helmholtz free energy and applied it to cooling channels in which the coolant is in a supercritical state. This approach is highly accurate, certainly better than using a cubic EoS, but numerically costly and thus currently not affordable for high-fidelity LES. As a remedy to this problem, Matheis *et al.*²⁰ identified various volume-translation methods for cubic EoSs and tested them in terms of modeling accuracy and numerical efficiency when used in both pressure- and density based CFD codes. By translating the thermodynamic state of the fluid along its volume axis, the prediction is considerably improved with minimal extra numerical effort. Two volume translations, the method of Harstad *et al.*²¹ (PR-VTH) and the method of Abudour *et al.*²² (PR-VTA), are used for the present simulations. Both are based on the PR EoS. The first method, PR-VTH, was already successfully applied in LES of supercritical mixing layers and trans- and supercritical nitrogen jets.^{23,24} The second method, PR-VTA, is introduced as a further improvement in terms of accuracy and modeling efficiency in the current contribution.

Modeling the subgrid-scale (SGS) stress tensor in the filtered LES transport equations is another aspect that needs to be addressed with particular care in trans- and supercritical flows. All well-established LES methods were originally developed in an incompressible or ideal-gas context and their applicability to simulations at supercritical pressures is therefore not necessarily given.²⁵ The lack of experimental data for turbulence quantities in high-pressure environments, however,

impedes the development of adapted SGS models and most groups thus resort to conventional closures. Park²⁶ and Petit *et al.*,²⁷ for instance, compared several SGS models in their simulations of the nitrogen jets of Mayer *et al.* Among them are the Vreman model²⁸ and the Smagorinsky model,²⁹ which both yield suitable results and are therefore used in the current contribution. In addition to these eddy-viscosity type models, we evaluate the Adaptive Local Deconvolution Method (ALDM)^{30,31} following an implicit LES approach. The key idea of the implicit SGS model, ALDM, is to combine turbulence modeling and robust numerical operators in a way that is consistent with turbulence theory.

A less often addressed topic is the role of the turbulent inflow boundary conditions in LES of trans- and supercritical flows. Simulations of jets in a low-pressure atmosphere yet showed that the location of break-up and spreading angle can be sensitive to the turbulent fluctuations that are prescribed at the inlet of the computational domain.³² For LES of supercritical jets, some groups^{27,33} used a mean velocity profile with superimposed turbulent fluctuations, while others^{23,24,34} performed a separate LES of the injector and interpolated cross-sectional slices of the velocity field onto the inlet plane of the jet simulation. Both methods assume that the injector is perfectly insulated or the wall having the same temperature as the injected fluid. The validity of this assumption was examined by Banuti and Hannemann³⁵ who performed RANS simulations for the experiments by Mayer *et al.*⁴ including the injector in their computational domain. Their results indicate that heat transfer from the injector wall to the cryogenic fluid may have a non-negligible influence on the jet dynamics. We therefore examine the influence of heat addition within the injector on LES predictions.

The remainder of this paper is divided into six sections: In Sec. II, we present the details of the numerical methods that are used in the current study. In Sections III and IV, the SGS turbulence and the real-gas thermodynamics models are introduced, respectively. The computational setup and the methods for generating turbulent inflow conditions are discussed in Section V. The results of the LES are presented in Section VI and compared with the experimental data. By discussing the influence of the different state-of-the-art modeling approaches, we contribute to a better understanding of the modeling requirements for cryogenic injection at supercritical pressures and to the further development of predictive CFD tools. Our conclusions are summarized in Section VII.

II. NUMERICAL METHOD

Two different CFD solvers will be used for this study: a pressure-based version of the open-source CFD package OpenFOAM (<http://www.openfoam.com>) and the density-based INCA (<http://www.inca-cfd.com>). Both codes solve for the compressible Navier-Stokes equations in conservation form

$$\frac{\partial \rho}{\partial t} + \frac{\partial (\rho u_i)}{\partial x_i} = 0, \quad (1a)$$

$$\frac{\partial (\rho u_i)}{\partial t} + \frac{\partial (\rho u_i u_j)}{\partial x_j} = -\frac{\partial p}{\partial x_i} + \frac{\partial \sigma_{ij}}{\partial x_j}, \quad (1b)$$

$$\frac{\partial (\rho e_t)}{\partial t} + \frac{\partial (\rho u_i e_t)}{\partial x_i} = -\frac{\partial (u_i p)}{\partial x_i} + \frac{\partial (u_i \sigma_{ij})}{\partial x_j} - \frac{\partial q_i}{\partial x_i}. \quad (1c)$$

Here, x_i are Cartesian coordinates, t is the time, ρ is the density, u_i is the velocity component in direction i , $e_t = e + u_i^2/2$ is the total energy, and p is the pressure. σ_{ij} and q_i represent the viscous stress tensor and heat flux, respectively. The viscous stress tensor for Newtonian fluids is

$$\sigma_{ij} = \mu \left(\frac{\partial u_i}{\partial x_j} + \frac{\partial u_j}{\partial x_i} - \frac{2}{3} \frac{\partial u_k}{\partial x_k} \delta_{ij} \right), \quad (2)$$

and heat conduction is modeled as

$$q_i = -\lambda \frac{\partial T}{\partial x_i}, \quad (3)$$

where μ and λ are the viscosity and thermal conductivity, respectively.

The codes differ in several aspects and are thus discussed separately in Subsections II A and II B. The thermodynamics as well as the boundary conditions are implemented consistently, cf. Sec. IV.

A. INCA

INCA is a flow solver for the compressible Navier-Stokes equations (1) in mass, momentum, and total energy conserving form. The governing equations are discretized on Cartesian grids with a conservative immersed boundary method^{36,37} and adaptive mesh refinement for the efficient representation of arbitrarily complex flow geometries. The viscous flux is discretized using a second-order central difference scheme and the third-order explicit Runge-Kutta scheme of Gottlieb and Shu³⁸ is used for time integration. We note that the Courant-Friedrichs-Lewy (CFL) condition for this conditionally stable time-marching method requires very small time steps in low Mach number flows.

INCA offers to model the effects of unresolved SGS turbulence both in an explicit and in an implicit manner. When used in an implicit LES mode, conservation equations (1) are solved directly and numerical discretization and physical modeling of unresolved SGS are fully merged. Effects of SGS turbulence are modeled by the ALDM of Hickel *et al.*,³¹ which provides the discretization of the inviscid flux. The method is detailed in Section III A.

Alternatively, INCA provides explicit turbulence models for the unresolved SGS. For the explicit LES discussed in this study, the inviscid flux is then discretized using second-order total-variation diminishing (TVD) schemes, where either the van Leer limiter³⁹ or the Koren limiter⁴⁰ is used to avoid unphysical oscillations at sharp density gradients. We also performed LES with the Superbee limiter,⁴¹ which, however, showed some spurious artifacts and will not be considered in the following. For explicit LES, Navier-Stokes equations (1) have to be filtered, which leads to

$$\frac{\partial \bar{\rho}}{\partial t} + \frac{\partial (\bar{\rho} \tilde{u}_i)}{\partial x_i} = 0, \quad (4a)$$

$$\frac{\partial (\bar{\rho} \tilde{u}_i)}{\partial t} + \frac{\partial (\bar{\rho} \tilde{u}_i \tilde{u}_j)}{\partial x_j} = -\frac{\partial \bar{p}}{\partial x_i} + \frac{\partial \bar{\sigma}_{ij}}{\partial x_j} - \frac{\partial \tau_{ij}}{\partial x_j}, \quad (4b)$$

$$\frac{\partial (\bar{\rho} \tilde{e}_t)}{\partial t} + \frac{\partial (\bar{\rho} \tilde{u}_i \tilde{e}_t)}{\partial x_i} = -\frac{\partial \tilde{u}_i \bar{p}}{\partial x_i} + \frac{\partial (\tilde{u}_i \bar{\sigma}_{ij})}{\partial x_j} + \frac{\partial (\tilde{u}_i \tau_{ij})}{\partial x_j} - \frac{\partial \bar{q}_i}{\partial x_i} - \frac{\partial \zeta_i}{\partial x_i}, \quad (4c)$$

where a bar $\bar{\star}$ denotes the finite-volume filter and a tilde denotes Favre filtering, that is, $\tilde{\star} = \overline{\rho \star} / \bar{\rho}$. The SGS fluxes $\tau_{ij} = \bar{\rho}(\tilde{u}_i \tilde{u}_j - \tilde{u}_i \tilde{u}_j)$ and $\zeta_i = \bar{\rho}(\tilde{u}_i \tilde{h} - \tilde{u}_i \tilde{h})$ in the filtered momentum and energy equation have to be modeled. Here, we employ two eddy-viscosity models: the Smagorinsky²⁹ and the Vreman models²⁸ which are discussed in Section III B. Weak nonlinearities of the filtered heat conduction \bar{q}_i and viscous stress $\bar{\sigma}_{ij}$ tensors are neglected; we directly compute them from the Favre filtered solution.

As highlighted by Selle *et al.*,²⁵ SGS terms that are negligible in a low-pressure atmosphere may become important in a transcritical environment. Their *a priori* LES study based on direct numerical simulations (DNSs) of supercritical mixing layers drew the attention to the difference between the filtered pressure gradient and the pressure gradient as computed from the filtered flow field as well as on the difference between the filtered heat flux and the heat flux computed from the filtered field. These terms can be significant in the filtered momentum and energy equation. A modeling approach (*p*-correction; *q*-correction) was proposed and tested in the following *a posteriori* LES study of the same group,^{42,43} showing a beneficial effect. Other groups, however, neglected the proposed *p*- and *q*-correction, referring to unsettled modeling issues, and yet obtained good results for LES of similar, inert configurations.^{13,27,33} In the present study, we also neglect these additional SGS terms. Furthermore, we calculate the thermodynamic and transport quantities using the filtered pressure and enthalpy, e.g., $C_p := C_p(\bar{p}, \tilde{h})$.

B. OpenFOAM

OpenFOAM is an open-source CFD software package that offers the flexibility to supplement the publicly available core code by additional features, e.g., real-gas thermodynamics or SGS models. It is based on a segregated, iterative solution approach and supports unstructured meshes.

Like in the explicit INCA simulations, we use second-order centered differences with a van Leer limiter³⁹ for spatial discretization. A first-order implicit Euler time integration scheme is used.

The OpenFOAM solver that is used in the current contribution is based on a *Pressure Implicit with Splitting of Operators* (PISO) algorithm and solves for filtered Navier-Stokes equations (4). Instead of solving for the continuity equation directly, the discretized momentum equation is used to derive a Poisson equation for the pressure, which guarantees mass conservation. Furthermore, the conservation law for the total energy $e_t = e + u_i^2/2 = h - p/\rho + u_i^2/2$ in Eq. (4c) is replaced by an energy equation in enthalpy form. The pressure and momentum equation is solved along with the enthalpy equation in a segregated approach, whereby a series of predictor-corrector steps is used to couple the fields. Originally designed for incompressible flows, the PISO algorithm is extended to allow for simulations of flows with moderate compressibility effects.^{44,45} The stiffness problem, which is a prominent drawback in the simulation of weakly compressible flows with density-based codes, does not apply — however, this comes on the cost of stability problems that arise from the sharp density gradients in supercritical simulations. Jarczyk and Pfizner²³ therefore proposed an adapted PISO algorithm, which significantly improves the solver behavior. The three major differences with respect to the classic ideal-gas approach as described by Issa *et al.*⁴⁴ are

- (a) The pressure transport equation is usually derived from the continuity equation and the discretized momentum equation assuming that the fluid is a perfect gas and thus the density a linear function of pressure. This assumption is violated when using a cubic EoS. The derivation is therefore adapted using a Taylor expansion to linearize the cubic EoS.
- (b) The thermodynamic properties of a fluid in a trans- or supercritical state are much more sensitive to the transported fields, i.e., pressure and enthalpy, than in subcritical environments. As a consequence, the respective transport equations are strongly coupled and it becomes necessary to incorporate both the enthalpy equation and the evaluation of the thermodynamic properties into the series of predictor-corrector steps.
- (c) Solving the transport equations sequentially implies that only the values of the transported field change, e.g., the enthalpy field is constant while solving the pressure equation. The compressibility $\psi = \partial \rho / \partial p$ in the pressure equation is therefore evaluated at isenthalpic conditions. The *isenthalpic compressibility* ψ_h deviates significantly from the commonly used *isothermal compressibility* ψ_T in the vicinity of the pseudo-boiling temperature.⁴⁶

With these modifications to the standard ideal gas approach in pressure-based algorithms, the pressure equation can be written as follows:

$$\frac{\partial (\bar{\rho}^0 - \tilde{\psi}_h^0 \bar{p}^0)}{\partial t} + \frac{\partial \tilde{\psi}_h^0 \bar{p}}{\partial t} + \frac{\partial}{\partial x_i} \left(\bar{\rho} \frac{H_p}{A_p} \right) - \frac{\partial}{\partial x_i} \left(\frac{\bar{\rho}}{A_p} \frac{\partial \bar{p}}{\partial x_i} \right) = 0. \quad (5)$$

The subscript 0 refers to the base point of the Taylor expansion that is used to linearize the EoS in the derivation. Typically, this point coincides with the solution at the previous time step. A_p denotes the coefficient matrix of the discretized momentum equation and H_p is an operator including the discretized source term. It is worth noting that the first term in the pressure equation is zero for perfect gases, but needed with real-gas thermodynamics models.

III. TURBULENCE MODELS

A. ALDM

The ALDM of Hickel *et al.*³¹ is a nonlinear finite volume reconstruction scheme and numerical flux function for implicit LES. Unlike explicit SGS models, implicit LES merges turbulence modeling and numerical discretization of the conservation equations. ALDM incorporates free parameters that control the implicit SGS model. An implicit SGS model that is consistent with turbulence theory was obtained through parameter calibration for canonical flows.^{30,31}

The compressible version of ALDM acknowledges that unresolved turbulence and discontinuities, such as shock waves and material interfaces, are fundamentally different flow phenomena and thus require different SGS modelings. Employing a flow sensor, ALDM captures strong

discontinuities without spurious oscillations and accurately represents smooth waves and turbulence without excessive numerical dissipation. A physically consistent implicit turbulence model implies a second-order modification in the governing equations. Hence, ALDM formally is a second-order discretization method whose truncation error is calibrated to act as a SGS turbulence model. When applied to linear waves, the methods yields a similar spectral resolution (modified wavenumber) as sixth-order central difference schemes.³¹ The ALDM flux function is low-Mach consistent, see the work of Hickel *et al.*,³¹ which is a prerequisite for the current application.

This numerical method has been proven particularly efficient for LES of shock-turbulence interaction^{47–49} and multiphase flows.^{50,51} For the application to transcritical flows, two adjustments were required. Because the previously used dilatation-vorticity sensor is not able to reliably detect strong density gradients in an only weakly compressible flow, we resorted to the sensor functional of Hill and Pullin,⁵² which directly evaluates the smoothness of the density field. Second, stable time integration is ensured by a positivity-preserving flux limiter.⁵³ This flux limiter is rarely active and used only for the very challenging transcritical case. Both methods are implemented in a straightforward way into the ALDM framework.

B. Eddy-viscosity models

We also apply two explicit SGS models, which both rely on the eddy-viscosity concept. In this framework, the SGS momentum and heat flux in Eqs. (4b) and (4c) are modeled as

$$\tau_{ij} = -2\mu_e \left(\tilde{S}_{ij} - \frac{1}{3} \tilde{S}_{kk} \delta_{ij} \right) + \frac{2}{3} \bar{\rho} k \delta_{ij}, \quad (6)$$

$$\zeta_i = -C_p \frac{\mu_e}{Pr_t} \frac{\partial \tilde{T}}{\partial x_i}, \quad (7)$$

with the rate of strain tensor

$$\tilde{S}_{ij} = \frac{1}{2} \left(\frac{\partial \tilde{u}_i}{\partial x_j} + \frac{\partial \tilde{u}_j}{\partial x_i} \right). \quad (8)$$

C_p is the isobaric heat capacity, which is modeled with real-gas thermodynamics models, and k is the SGS turbulence kinetic energy. The turbulent Prandtl number Pr_t is set to 1 for the present simulations. We should add that, though very common, assuming a constant turbulent Prandtl number is a strong assumption. Experiments and DNS support values ranging from $Pr_t = 0.35$ to $Pr_t = 4$ and there are indications that Pr_t can even have negative values in particular cases.⁵⁴ The SGS viscosity μ_e is modeled using either the Smagorinsky model²⁹ or the Vreman model.²⁸

1. Smagorinsky model

The Smagorinsky²⁹ model for the SGS viscosity is

$$\mu_e = c_k \Delta \bar{\rho} \sqrt{k}, \quad (9)$$

where k denotes the SGS turbulence kinetic energy and Δ is the filter size. The SGS viscosity can be calculated from Eq. (6) by assuming local equilibrium, i.e.,

$$\tau_{ij} \tilde{S}_{ij} = -c_e / \Delta \bar{\rho} k^{3/2}. \quad (10)$$

The model constants are $c_k = 0.02$ and $c_e = 1.048$.

2. Vreman model

Vreman²⁸ proposed the following model for the SGS viscosity:

$$\mu_e = c_v \bar{\rho} \sqrt{\frac{B_\beta}{\alpha_{ij} \alpha_{ij}}}, \quad (11)$$

with

$$B_\beta = \beta_{11}\beta_{22} + \beta_{11}\beta_{33} + \beta_{22}\beta_{33} - \beta_{12}^2 - \beta_{13}^2 - \beta_{23}^2, \quad (12a)$$

$$\beta_{ij} = \Delta^2 \alpha_{ki} \alpha_{kj}, \quad (12b)$$

$$\alpha_{ij} = \frac{\partial \tilde{u}_j}{\partial x_i}. \quad (12c)$$

The tensor β is proportional to the gradient model of Clark *et al.*⁵⁵ — a desirable feature since Selle *et al.*²⁵ found that the gradient model outperforms most other models for supercritical mixing layers. The model coefficient is $c_v = 0.07$.

Compared to the Smagorinsky model, Vreman's approach has the advantage that the SGS viscosity vanishes in laminar flows. The isotropic part of the SGS stress tensor in Equation (6) is neglected for both SGS models since it was found to be small compared to the fluctuations of the thermodynamic pressure.^{56,57}

IV. THERMODYNAMICS MODELS

A. Equation of state

It is well known that a fluid can be described with the ideal gas EoS only in a low pressure environment. As the pressure approaches and exceeds the fluid's critical value, intermolecular forces become increasingly important and have to be considered. An established method is the corresponding states principle,⁵⁸ in which the relation between the thermodynamic state variables is described in terms of normalized or *reduced* variables. The reduction parameters are the critical properties of the fluid, i.e., the critical temperature T_c , pressure p_c , and specific volume v_c . The EoS has then a universal character and can be cast into a cubic, van der Waals like form using free parameters to model the deviation from the perfect gas assumption. One example is the well-known PR EoS,

$$p = \frac{RT}{v_{PR} - b} - \frac{a}{v_{PR}^2 + 2v_{PR}b - b^2}, \quad (13)$$

which employs parameters to describe the intermolecular forces, the deviation from a circular molecular shape, and the reduction of free volume due to the finite volume of the molecules. The molar volume is denoted by v_{PR} and R is the molar gas constant. Intermolecular attractive forces are described by the temperature dependent function a and the reduction of free volume by b . Both functions are empirical and normalized to the critical point of the fluid they describe,

$$a = 0.457 \frac{R^2 T_c^2}{p_c} \left(1 + \kappa \left(1 - \sqrt{\frac{T}{T_c}} \right) \right)^2, \quad (14)$$

$$b = 0.0778 \frac{RT_c}{p_c}. \quad (15)$$

The function $\kappa = 0.37464 + 1.54226\omega - 0.26992\omega^2$ accounts for the deviation of the molecules from a perfect circular shape. ω denotes the constant eccentric factor ($\omega_{N_2} = 0.037$).

In order to close the set of balance equations (1) and (4), relations for the thermodynamic quantities need to be derived in terms of the transported fields. Which quantities are needed depends on the code architecture, i.e., whether a density-based or a pressure-based approach is chosen, and on the choice of the transported fields. While OpenFOAM (pressure-based) needs thermodynamic relations for the enthalpy h , the isenthalpic compressibility Ψ_h , and the isobaric heat capacity c_p , INCA (density-based) uses the total energy e_t , the isochoric heat capacity c_v , and the speed of sound a_s (which depends on the ratio of c_p and c_v). All of these quantities can be derived from the PR EoS and a formulation for the Gibbs free energy, i.e., a caloric EoS,

$$g(T, p) - g^0(T) = \int_{p_0}^p \left(v_{PR} - \frac{RT}{p} \right) dp. \quad (16)$$

The superscript 0 refers to standard conditions ($p_0 = 1$ bar) and the reference Gibbs free energy g^0 is calculated using the 9-coefficient NASA-polynomials proposed by Goos *et al.*⁵⁹ The pressure-dependent real-gas correction term on the right side can be evaluated using the PR EoS. The expressions derived for the thermodynamic quantities mentioned above are given in [Appendix A](#).

The molecular transport properties, i.e., the viscosity and the thermal conductivity, are modeled with the empirical correlation for dense fluids of Chung *et al.*⁶⁰ as described in [Appendix B](#).

B. Volume-translation methods

Cubic EoSs have deficiencies in predicting liquid densities, especially at operating conditions close to the critical point. This is mainly attributed to their inability to predict the fluid's critical compressibility factor $Z_c = (p_c v_c)/(RT_c)$ correctly.^{22,61} In particular, two-parameter EoSs, such as the PR EoS, yield a constant critical compressibility factor for all species. This results in modeling errors in the vicinity of the critical point, whose severity depends on the considered species. For instance, the measured critical compressibility factor of nitrogen is $Z_c^{N_2} = 0.289$ and thus considerably smaller than the value predicted by the PR EoS $Z_c^{PR} = 0.3074$. Despite such uncertainties, the PR EoS appears to be a good choice when compared to other EoSs, such as Soave-Redlich-Kwong $Z_c^{SRK} = 0.333$, van der Waals $Z_c^{vdW} = 0.375$, or ideal gas $Z_c^{IG} = 1$. Nevertheless, this deficiency initiated the development of *volume-translation* methods as originally suggested by Martin.⁶² They are based on a translation of the thermodynamic state along the volume axis to improve the liquid density predictions. Several approaches of varying complexities and accuracy were proposed, two of which are tested for the current simulations.

1. Method of Harstad *et al.*²¹ (PR-VTH)

Harstad *et al.*²¹ developed a thermodynamically consistent volume translation method. Thermodynamic consistency means that the resulting caloric and thermal EoS can be expressed in canonical form. This is a desirable feature, which is often abandoned in other volume-translation methods for the benefit of simplicity and higher accuracy of the thermal EoS.²⁰ Harstad *et al.*²¹ proposed a model for the Gibbs free energy at standard conditions g^0 , Eq. (16), rather than for the volume translation itself. The real-gas departure function is thereby evaluated using the PR EoS, whereas the value of g is determined from highly accurate correlations. For g^0 , they propose an empirical function that is both pressure and temperature dependent and contains 20 species-specific, empirical constants that are calibrated with a curve fitting method. The amount by which the thermodynamic state is shifted along the volume axis is then determined as the derivative of the standard Gibbs free energy with respect to pressure. The corrected molar volume,

$$v = v_{PR} + \left. \frac{\partial g^0}{\partial p} \right|_T, \quad (17)$$

is the sum of the contributions from the PR EoS and the volume translation. For the present simulations, we use the volume shift proposed by Harstad *et al.*²¹ and their empirical function for g^0 . The caloric properties, i.e., e_t and h , are calculated using the caloric EoS as described in [Sec. IV A](#).

2. Method of Abudour *et al.*²² (PR-VTA)

Abudour *et al.*²² developed a generalized form of the volume-translation method of Chou and Prausnitz,⁶³ who proposed to parameterize the volume shift based on a dimensionless distance function,

$$d = - \frac{v_{PR}^2}{RT_c} \left. \frac{\partial p}{\partial v_{PR}} \right|_T, \quad (18)$$

between the critical point and the pressure-density isotherm. The translated volume is the sum of the contributions of the PR EoS and the volume translation

$$v = v_{PR} + c + \delta_c \left(\frac{0.35}{0.35 + d} \right), \quad (19)$$

where the function

$$\delta_c = \frac{RT_c}{p_c} (Z_c^{PR} - Z_c) \quad (20)$$

accounts for the deviation of the EoS's critical compressibility factor prediction. An expression for c is given as

$$c = \frac{RT_c}{p_c} (c_1 - (0.004 + c_1) e^{-2d}), \quad (21)$$

with

$$c_1 = 0.4266Z_c - 0.1101. \quad (22)$$

This method contains no empirical fluid-dependent fitting parameter and is yet highly accurate. However, we (and others) were not able to find an analytical solution for the integral in the real-gas departure function, Eq. (16), with the volume translation of Abudour *et al.* and the computational cost of numerical integration within the iterative solution procedure turned out to be intractable in the framework of high-fidelity CFD.²⁰ That is, it is presently not possible to use this volume-translation method for our purposes in a fully thermodynamically consistent way. In practice, we therefore resort to the untranslated volume for the evaluation of the departure function. The effect on the predictions was found to be very small, and this weak inconsistency is tolerated for the sake of a highly accurate and numerically efficient thermal EoS.^{20,34}

C. Verification of real-gas thermodynamics

Figure 1 compares the thermodynamic models against highly accurate reference data from the NIST chemistry webbook¹⁷ for nitrogen at a pressure of 4 MPa. The NIST reference data are based on the EoS of Span *et al.*⁶⁴ This comparison clearly demonstrates the benefit of the volume-translation methods. Especially at low temperatures, here $T < 120$ K, the unmodified PR EoS significantly overpredicts the density. This can be corrected with either of the two proposed volume translations. In particular, the Abudour correction shows excellent agreement with the NIST data.

The heat capacity has a sharp peak at the pseudo-boiling temperature ($T_{pb} = 129.6$ K), a feature that is nicely recovered by the PR EoS. As mentioned before, it is not feasible to include the volume translation of Abudour *et al.*²² in the caloric EoS and thus, no corrected results are shown for the heat capacity, the compressibility, or the speed of sound, which all need caloric properties in their evaluation. The Chung model,⁶⁰ which is used for the viscosity μ and the thermal conductivity λ , however, explicitly depends on the fluid molar volume. The translation methods' influence is thus considered and proves beneficial.

The compressibility is compared with the reference data both for isenthalpic and isothermal conditions, both showing good agreement. Like the heat capacity, the compressibility exerts a peak at the pseudo-boiling temperature if evaluated at isothermal conditions. This feature is strongly alleviated at isenthalpic conditions. As already mentioned in Sec. II B, using ψ_h is indispensable for the numerical stability of the real-gas pressure-based solution algorithm that solves the energy equation in enthalpy form.

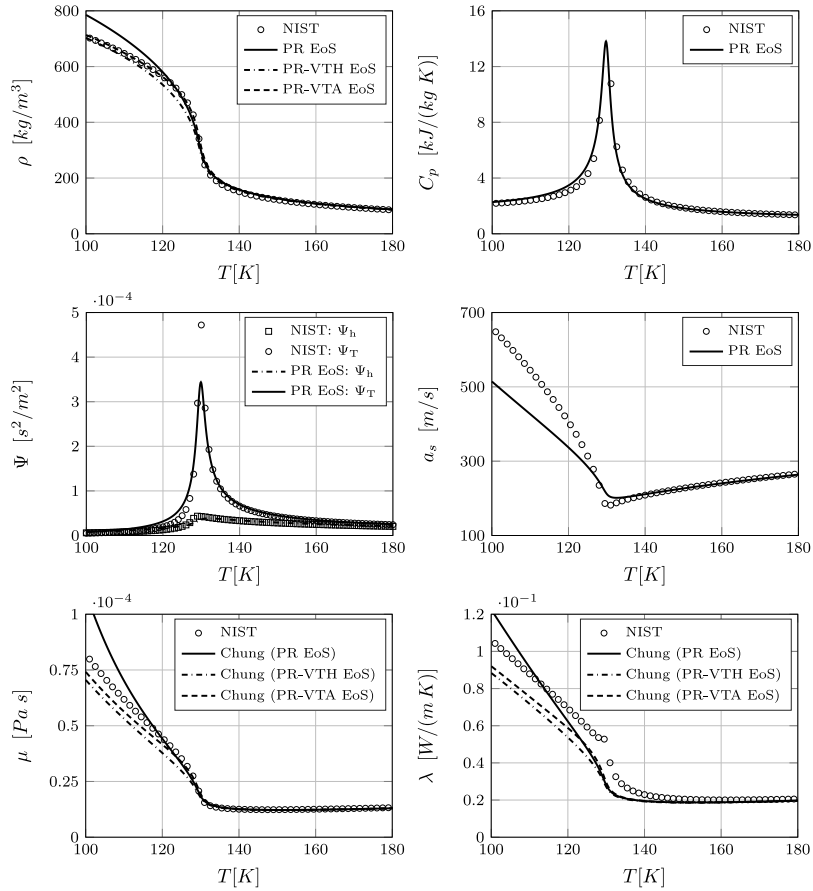


FIG. 1. Verification of the real-gas thermodynamics models for N_2 at $p = 4$ MPa with respect to the NIST¹⁷ reference data.

V. EXPERIMENTAL AND COMPUTATIONAL SETUP

A. Reference experiment

We test the thermodynamics and turbulence models as well as the numerical techniques against the experimental database of Mayer *et al.*,⁴ who conducted an extensive series of measurements for injection at supercritical pressures. Cold nitrogen is injected into a cylindrical chamber that is initially filled with warm nitrogen ($T_{ch} = 298$ K) at pressures varying between 3.95 MPa and 5.98 MPa. The jet bulk velocities vary between 1.8 m/s and 5.4 m/s. The temperatures of the injected nitrogen are between 122 K and 140 K, hence enclosing the pseudo-boiling temperature at the respective operating pressures. As a consequence, the cold nitrogen is injected either in a trans- or in a supercritical state, according to the case considered, while the nitrogen in the chamber is always supercritical. The injector diameter is $D = 2.2$ mm. The diameter of the chamber is 122 mm and its length is 1 m.

We confine our study to case 3 and case 4 of the experiments by Mayer *et al.*⁴ Both cases have similar chamber pressures and injection velocities but differ in the injection temperature. In particular, the injection temperatures lie on either side of the pseudo-boiling temperature, with the injected nitrogen in case 3 being in a transcritical and in case 4 in a supercritical state. As a consequence, the nitrogen density differs significantly, even though the measured temperature difference is only 10 K. The experimental testing conditions are summarized in Table I.

Despite the sophisticated measurement techniques that were used by Mayer *et al.*,⁴ they report difficulties in determining the exact temperature of the injected fluid. They argue that due to heat addition in the injector, the temperature field at the injector exit may be not well defined with a single measured value. Together with the severe impact on the density, see Fig. 1, this adds some

TABLE I. Operating conditions of Mayer *et al.*⁴ experiment.

	Case 3	Case 4
Injection velocity (m/s)	4.9	5.4
Chamber pressure (MPa)	3.97	3.98
Injection temperature (K)	126.9	137
Injection Reynolds number ^a	1.62×10^5	1.53×10^5
Injection Mach number ^a	0.019	0.027

^aCalculated using NIST.¹⁷

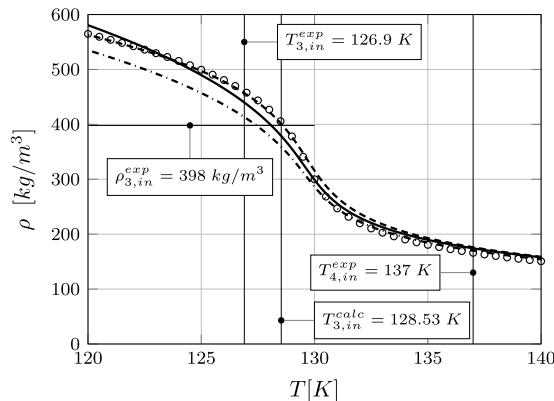
uncertainty in the LES. We thus employ an alternative approach to determine the temperature at the injector exit, taking the Raman-2D density measurements as a reference. By averaging the experimental data points in the section prior to jet break-up, an experimental value for the mean density at the injector exit can be estimated. For case 3, this is $\rho_{3,in}^{exp} = 398 \text{ kg/m}^3$ as illustrated in Fig. 2. With a highly accurate equation of state, as available in the NIST chemistry webbook,¹⁷ the injection temperature for case 3 can then be calculated as $T_{3,in}^{calc} = 128.53 \text{ K}$. Even though the difference to the thermocouple measurement is only $\Delta T_{in} = 1.55 \text{ K}$, it implies a density variation of $\Delta \rho_{in} = 56.8 \text{ kg/m}^3$. We believe that using the calculated inlet temperature allows for a better assessment of the thermodynamic models, especially of the EoS, since ambiguities that arise from inconsistencies between measured inlet temperature and density are avoided. For instance, an EoS that under predicts the density at the measured injection temperature by the mentioned 56.8 kg/m^3 would perfectly match the experiment, whereas an accurate EoS would fail by the same amount.

B. Turbulent inflow boundary conditions

In LES, important characteristics of turbulent jet flows, such as location of jet break-up and spreading angle, may depend on the method with which the turbulent inflow boundary condition is generated.³² We employ two methods, which are described in the following.

1. Incompressible constant-density pipe flow with adiabatic walls (P-CD)

First, a separate incompressible LES of a turbulent constant-density pipe flow is carried out using OpenFOAM. Cyclic boundary conditions are used in the axial direction and a pressure gradient is enforced to maintain the prescribed bulk velocity. The pipe wall is adiabatic in this simulation and thus, no energy transport is considered. The pipe-flow mesh contains $450 \times 40 \times 120$ grid points in axial, radial, and circumferential directions, with gradual grid refinement applied towards the wall. The pipe diameter ($D = 2.2 \text{ mm}$) and the bulk velocity as well as the Reynolds number

FIG. 2. Inlet conditions for the current simulations. \circ : NIST, —: PR EoS, ---: PR-VTH EoS, ···: PR-VTA EoS.

correspond to the experiments by Mayer *et al.*⁴ (see Table I); the length of the periodic pipe section is $x/D = 10$. The Vreman model is used for closing the LES equations.

This LES is used to extract slices of the instantaneous turbulent velocity field and store them in a database. These data are later interpolated onto the grid and time step of the jet simulation. This method is numerically expensive when compared to other conventional approaches, which typically use correlations for the mean velocity profile and superimpose fluctuations.²⁷ It is yet accurate, if the Mach number is small and wall heat transfer is negligible. The latter is not necessarily given in the jet experiments of Mayer *et al.*^{4,7,35} In particular, the laser signal was recorded in a transient phase, in which the injected fluid was used to chill down the feeding lines of the experimental facility. A turbulent temperature profile is thus expected at the injector exit, with the lowest temperature at the pipe center and the highest at the wall. This makes the incompressible method questionable, especially if one considers the strong density-temperature coupling at the present operating conditions. We therefore generate a second set of turbulent inflow boundary conditions that account for heat transfer from the injector wall to the fluid.

2. Compressible pipe flow with isothermal walls (P-VD)

In the second approach, we perform a compressible LES of a pipe flow with isothermal walls using OpenFOAM. The velocity database of the foregoing incompressible LES is interpolated onto the inlet of this second pipe segment. The pipe dimension as well as the grid resolution coincides with the incompressible simulation; however, non-periodic inflow and outflow boundary conditions are used. To account for the heat flux originating from the isothermal walls, the enthalpy balance equation is solved along with the momentum and the pressure equation using the PR-VTA EoS and the Vreman SGS model. In order to determine a realistic temperature boundary condition for the injector wall, we performed a separate conjugate heat transfer computation (not shown). The resulting wall temperature is estimated as $T_w = 240$ K. The bulk temperature at the pipe inlet as well as the pressure at the outlet correspond to the setup of Mayer *et al.*⁴ (see Table I). Note that the Reynolds number does not remain constant due to the heat addition and the corresponding expansion. Slices of both the turbulent temperature and the turbulent velocity field are extracted at the axial position $x/D = 10$ and stored in a database, which is later used to simulate the jet flow.

3. Precursor pipe-flow results

The averaged results of the incompressible simulations with constant density (P-CD) are compared with the heated, compressible pipe flow results (P-VD) at two axial positions. The setup corresponds to case 3 of Mayer *et al.*,⁴ i.e., the pressure at the pipe exit is $p = 3.97$ MPa, the bulk velocity is $\bar{U} = 4.9$ m/s, and the inlet temperature is $T = 128.53$ K. The results are averaged over 40 flow through times and 60 circumferential positions. Figure 3 shows the averaged density profiles and Root-Mean-Square (RMS) density fluctuations in a wall-normal direction; $r/R = 1$ corresponds to the wall, $r/R = 0$ to the pipe center, with $R = D/2 = 1.1$ mm. Since the inlet- and the wall temperature enclose the pseudo-boiling temperature of nitrogen at this pressure ($T_{pb} = 129.6$ K), the heat addition leads to a severe expansion near the wall. At the same time, the pseudo-boiling process leads to the formation of a wall-normal layer in which the heat capacity reaches very high values (cf. Fig. 1). Wall-normal heat conduction is thus inhibited and the evolution of the thermal boundary layer is deferred in comparison to pipe flows at lower pressures. The density fluctuations are confined to a layer close to the wall, even at $x/D = 10$.

Figure 4 shows mean profiles for the averaged axial velocity component as well as the radial and axial Reynolds stresses and the Reynolds shear stress. The expansion leads to an acceleration of the mean flow. In addition, the turbulent fluctuations are strongly affected by the wall-normal density gradient. Both the axial and the wall-normal fluctuations are effectively damped by the heat addition, an effect which is also found on the surface of supercritical, cryogenic jets, see the work of Zong *et al.*¹⁰ Wall-normal turbulent heat transport is thus reduced and the evolution of the thermal boundary layer is further delayed. Note that the turbulent properties reflect only the fluctuations on the resolved scales, the modeled SGS turbulence is not considered.

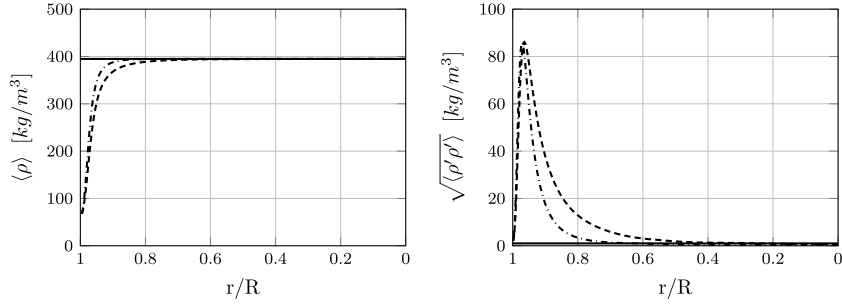


FIG. 3. Profiles of mean density and RMS density for N_2 at $p = 3.97$ MPa in a pipe. — : Adiabatic wall, - - - : $T_w = 240$ K; $x/D = 5$, - · - : $T_w = 240$ K; $x/D = 10$.

C. Computational domain

The grid used in OpenFOAM is axisymmetric and stretched in radial and in axial directions, whereas a block-structured Cartesian grid is used in INCA. The discretized domains for the simulations are shown in Fig. 5. The OpenFOAM grid comprises 4.21×10^6 finite volumes and the injector plane is resolved with 1840 cells. The smallest cell size in radial direction is $6.2 \mu\text{m}$. In order to study whether these grids are sufficient for the following parameter study, we performed a grid convergence study using the OpenFOAM solver, where the base grid was uniformly refined and coarsened in all three spatial directions. The coarsened grid comprises of 2.12×10^6 and the refined grid of 8.38×10^6 cells. Figure 6 demonstrates the influence of the grid resolution on the mean density profiles on the centerline of the jet. It can be observed that the sharp density decreases after break-up is better resolved on the medium and fine grid and its location is slightly shifted upstream. The results show a clear indication of grid convergence, i.e., the difference between the fine grid and the base grid is small enough to consider the results obtained with the base grids reliable.

We compare INCA and OpenFOAM simulations that correspond to roughly the same computational cost and exploit the advantages of the particular solver, which implies different grid topologies. The adaptive Cartesian grid used in INCA consists of 2.36×10^6 finite volumes and the

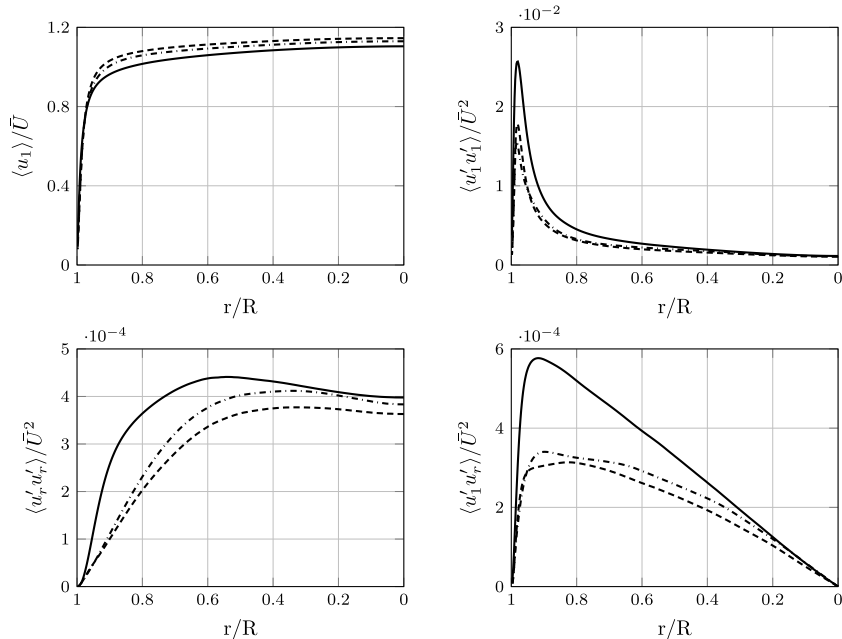


FIG. 4. Profiles of mean velocity, radial, and axial Reynolds stresses and Reynolds shear stress for N_2 at $p = 3.97$ MPa in a pipe. — : Adiabatic wall, - - - : $T_w = 240$ K; $x/D = 5$, - · - : $T_w = 240$ K; $x/D = 10$.

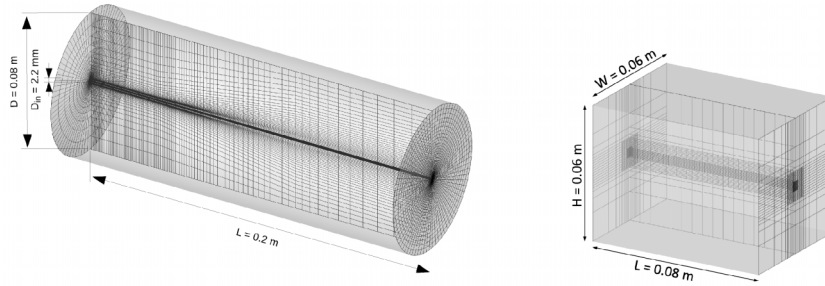


FIG. 5. Numerical domains used for the simulations with OpenFOAM (left) and INCA (right), every fourth grid line is shown.

injector plane is resolved with approximately 800 cells. These cells have a quadratic cross section with a side length of $68.8 \mu\text{m}$ in both cross-stream directions in the area close to the centerline of the jet and they are coarsened in regions further away from the centerline than one injector diameter.

D. Simulated operating points

In the following, we perform a parameter study to provide a thorough overview on the influence of thermodynamics modeling, turbulence modeling, numerical methods, and inflow conditions on the LES results for the present test cases. We therefore conduct a series of simulations (see Table II) that allows to distinguish the influence of the mentioned parameters. Based on setup Case3-1 (P-CD; $T_{in} = 128.53 \text{ K}$), we study the influence of heat transfer from the injector wall to the injected fluid as well as the uncertainty in the temperature measurements by comparison with Case3-2 (P-CD; $T_{in} = 126.9 \text{ K}$) and Case3-3 (P-VD; $T_{in} = 128.53 \text{ K}$). The role of using volume-translation methods is studied by comparing Case3-1 (PR-VTA) with Case3-8 (PR) and Case3-9 (PR-VTH). This is done using the OpenFOAM solver. INCA is used to study the influence of SGS modeling based on Case3-4 (ALDM), Case3-5 (Vreman), and Case3-6 (Smagorinsky). To quantify the effect of numerical diffusion that stems from the TVD discretization of the nonlinear advection term, we discuss results for explicit LES with two different TVD limiters: Case3-5 van Leer³⁹ limiter, which is also used in the OpenFOAM implementation, and Case3-7 with the less dissipative Koren⁴⁰ limiter. In addition to these transcritical test cases, we perform simulations for supercritical injection conditions, case 4 of Mayer *et al.*,⁴ and study the effect of the numerical method by comparing Case4-1 (OpenFOAM; Vreman), Case4-2 (INCA; ALDM), and Case4-3 (INCA; Vreman) in a situation where the density stratification is considerably smaller than in the foregoing parameter study.

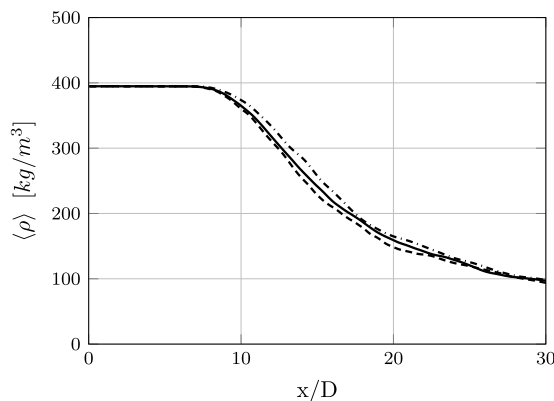


FIG. 6. OpenFOAM grid study for mean density profiles on the jet centerline for case 3. - - - : Coarse (2.12×10^6 cells), — : base (4.21×10^6 cells), - . - : fine (8.38×10^6 cells).

TABLE II. Boundary conditions for the present simulations.

	Code	Inflow	T_{in} , (K)	SGS model/flux limiter	EoS
Case3-1	OpenFOAM	P-CD ^a	128.53 ^b	Vreman/van Leer	PR-VTA ^c
Case3-2	OpenFOAM	P-CD	126.9 ^d	Vreman/van Leer	PR-VTA
Case3-3	OpenFOAM	P-VD ^e	128.53	Vreman/van Leer	PR-VTA
Case3-4	INCA	P-CD	128.53	ALDM	PR-VTA
Case3-5	INCA	P-CD	128.53	Vreman/van Leer	PR-VTA
Case3-6	INCA	P-CD	128.53	Smagorinsky/van Leer	PR-VTA
Case3-7	INCA	P-CD	128.53	Vreman/Koren	PR-VTA
Case3-8	OpenFOAM	P-CD	128.53	Vreman/van Leer	PR ^f
Case3-9	OpenFOAM	P-CD	128.53	Vreman/van Leer	PR-VTH ^g
Case4-1	OpenFOAM	P-CD	137.0 ^d	Vreman/van Leer	PR-VTA
Case4-2	INCA	P-CD	137.0	ALDM	PR-VTA
Case4-3	INCA	P-CD	137.0	Vreman/van Leer	PR-VTA

^aIncompressible pipe flow with constant density (see Sec. V B 1).

^bValue calculated from measured density using NIST.¹⁷

^cPeng-Robinson EoS with Abudour correction (see Sec. IV B 2).

^dValue measured by Mayer *et al.*⁴

^eCompressible pipe flow with variable density profile (see Sec. V B 2).

^fUncorrected Peng-Robinson EoS (see Sec. IV A).

^gPeng-Robinson EoS with Harstad correction (see Sec. IV B 1).

We finally compare the results for transcritical (Case3-1 and Case3-5) with those of supercritical injection (Case4-1 and Case4-3) using the same TVD limiter and SGS model.

VI. RESULTS

A. Instantaneous flowfield

The upper part of Fig. 7 shows instantaneous LES realizations of the density gradient magnitudes in a plane perpendicular to the inflow direction. The color-map scaling is exponential. The black isolines refer to the arithmetic mean density between the injector exit and the surrounding nitrogen ($\hat{\rho} = 0.5(\rho_{in} + \rho_{\infty})$) and illustrate the potential core and the location of jet break-up. A comparison of instantaneous realizations is admittedly qualitative, yet well suited to demonstrate the differences between trans- and supercritical injections. In setup Case3-1, the injection temperature lies below the pseudo-boiling temperature and the near-injector flow field is thus characterized by a sharp density gradient that encloses the cold jet. We find maximum values of the density gradient that are three times higher than in Case4-1. The large density stratification between jet core and surroundings hinders the formation of Kelvin-Helmholtz type vortices and therefore delays the jet break-up. Zong *et al.*¹⁰ argued that in this area, strong local anisotropies transfer turbulence kinetic energy from a direction perpendicular to the jet surface to the streamwise direction. This wall-like behavior is clearly visible in the structure of the jet surface closely downstream of the injector ($x/D < 5$). While for setup Case4-1, coherent vortices evolve close to the injector eventually leading to jet break-up, the jet surface stays rather undisturbed in this section for Case3-1. In addition, it can be observed that dense pockets of cold nitrogen are separated from the main jet. They are swept further downstream and eventually mix with the surrounding warm nitrogen and dissolve. The location at which the pockets separate stays rather constant during the simulated temporal evolution. It is $x/D \approx 10$ for Case4-1 and $x/D \approx 15$ for Case3-1.

It was already mentioned that the pseudo-boiling process is connected to a peak of the isobaric heat capacity value, see Fig. 1. This effect is recovered in the LES as shown in the lower part of Fig. 7. The instantaneous C_p -field of Case3-1, in which the pseudo-boiling temperature T_{pb} is surpassed during heat-up, is fundamentally different from that of Case4-1 where the injection temperature is higher than T_{pb} . Case3-1 features a layer of high heat capacity at the jet interface.

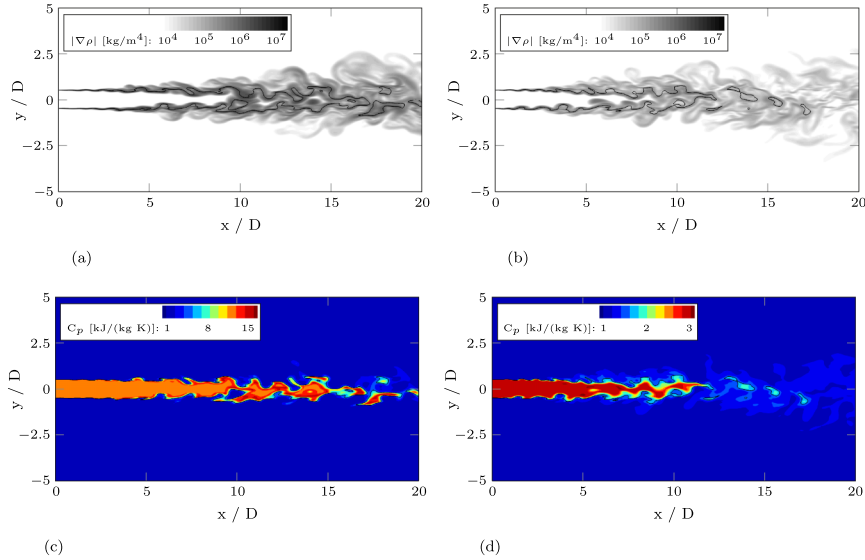


FIG. 7. Snapshots of the density gradient magnitude (top) and isobaric heat capacity (bottom) of Case3-1 (left) and Case4-1 (right). The black isoline denotes the arithmetic mean density between inlet and ambient nitrogen $\bar{\rho} = 0.5(\rho_{in} + \rho_{\infty})$. (a) Case3-1: Density gradient magnitude. (b) Case4-1: Density gradient magnitude. (c) Case3-1: Heat capacity at constant pressure. (d) Case4-1: Heat capacity at constant pressure.

This layer acts as a *heat shield*, meaning a higher amount of energy is needed to produce a temperature increase. A further stabilization of the jet's dense core is the result, since the effect impedes the distortion of the sharp density gradient. This stabilizing layer is missing when the injected fluid is in a purely supercritical state.

B. Mean flow

Figure 8 shows experimental and numerical data for the averaged density on the jet centerline. In the LES, temporal averaging was started after the flow field was considered fully developed in the region of interest and then continued for $\Delta t = 400D_{in}/U_{in} \approx 0.18$ s. The axisymmetric density data of Mayer *et al.*⁴ for case 3 are rather constant prior to jet break-up at $x/D < 10$ followed by a strong, constant-rate decrease between $10 < x/D < 17$. A slope discontinuity can be observed at $x/D \approx 17$. The density further decreases thereafter eventually reaching the warm nitrogen density.

Figure 8(a) compares the simulation results for different inflow conditions. For setup Case3-1 and Case3-2, we interpolate the turbulent velocity field as obtained from an incompressible pipe flow onto the jet inflow plane, see Sec. V B 1. The uniform temperature is $T_{in} = 128.53$ K for Case3-1 and $T_{in} = 126.9$ K for Case3-2 and corresponds to the calculated and the measured value, respectively. In Case3-3, we consider heat addition at the injector wall. Both the velocity and the temperature field are thus extracted from a compressible pipe flow simulation at the axial position $x/D = 10$, see Sec. V B 2. Comparing the results of setups Case3-1 and Case3-3, we find that the influence of heat addition in the injector on the averaged density profiles is negligible in this configuration. The difference between the simulations with the calculated and the measured temperature, i.e., Case3-1 and Case3-2, is yet clear. Case3-1, in which the temperature is adjusted to match the experimental density, is in excellent agreement with the measurements, whereas Case3-2 shows distinct deviations. In the region prior to jet break-up, this can be explained with the inconsistency between the measured inflow temperature and the density as mentioned earlier. However, an offset remains even in the fully turbulent region of the jet, where the dependence between temperature and density is less pronounced. The sudden change of the slope, which can be observed in the experiment at $x/D \approx 17$, is nicely recovered in the simulations that use the calculated temperature. For Case3-2, its location is shifted downstream to $x/D \approx 21$.

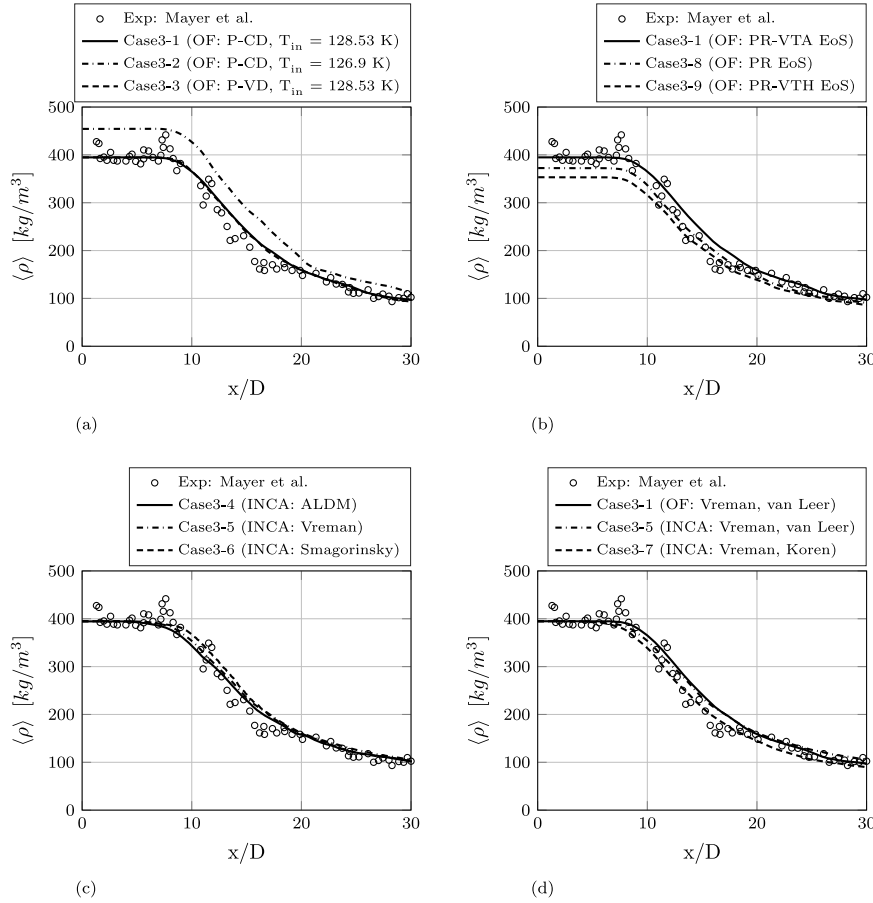


FIG. 8. Profiles of mean density on the jet centerline for case 3. (a) Influence of the inflow condition. (b) Influence of volume translation. (c) Influence of SGS modeling. (d) Influence of numerical method.

The volume-translation methods that were presented in Sec. IV B are compared with the uncorrected PR EoS in Fig. 8(b). In all three simulations, we use the Vreman SGS model and the re-calculated inlet temperature $T_{in} = 128.53$ K. Thus, the difference between the respective methods in the section prior to break-up can purely be attributed to the volume-translation method. The method of Abudour *et al.*²² matches the experimental data in the potential region and in the region after the slope change, whereas the uncorrected PR EoS and the PR-VTH EoS under-predict the density considerably. In particular, using the volume-translation method of Harstad *et al.*²¹ has an adverse effect compared to the uncorrected PR EoS for this particular operating point. This is in agreement with the results presented in Fig. 2. Furthermore, we observe that the density offset persists beyond the slope discontinuity at which the temperature is significantly increased due to mixing with the warm surrounding. The influence of the volume-translation methods vanishes at higher temperatures, see Fig. 1. However, the choice of the volume-translation method also affects the evolution of the flow field after the jet break-up. The differences between the density predictions in this region is attributed to non-local, non-linear effects of the EoS formulation on the flow evolution. We assume that this is a result of the impact on the mass flow as well as of the interplay between density gradient and turbulent fluctuations on the jet surface, as will be shown in Sec. VI C.

Figure 8(c) shows the influence of the different SGS models used in this study on the mean density prediction. ALDM and Vreman model yield very similar density profiles, whereas the jet break-up is shifted downstream for the Smagorinsky model. The advantage of the Vreman model over the Smagorinsky model (to switch itself off in laminar regions, in particular on the jet surface)

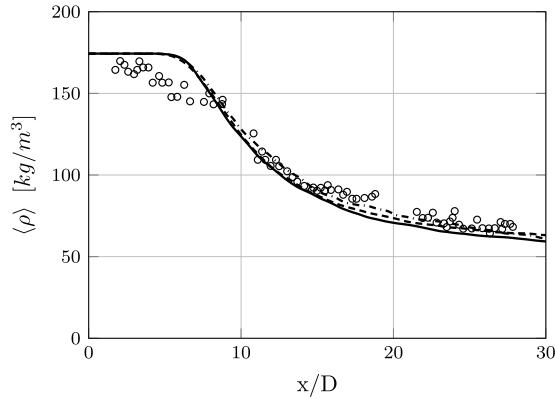


FIG. 9. Profiles of mean density on the jet centerline for case 4. \circ : Experimental data,⁴ LES results for — : Case4-1 (OpenFOAM: Vreman), - - - : Case4-2 (INCA: ALDM), - . - : Case4-3 (INCA: Vreman).

does notably improve the results for this configuration. All models yield a very similar mean density evolution in the far field $x/D > 20$.

The effect of numerical diffusion on LES with the Vreman SGS model is evaluated in Fig. 8(d). With INCA, artificial diffusion predominantly stems from the TVD discretization of the nonlinear advection term. With OpenFOAM, the implicit time integration method contributes additionally. Comparing the results for the limiters of van Leer and Koren, we clearly see that numerical diffusion delays break-up and mixing. This is because the more restrictive van Leer limiter damps the physical instabilities eventually leading to turbulence. The mean density profile for OpenFOAM agrees very well with the INCA prediction obtained with the identical flux limiter, although the computational grids differ considerably.

Drawing a first conclusion on the relative importance of the considered parameters, we observe that the choice of the thermodynamics model and in particular the accurate prediction of the fluid's thermodynamic state in the transcritical region had a significant effect not only on the potential region of the jet but also on the far field. The same holds for the injection temperature, for which a change of less than 2 K resulted in a considerable variation of the flow field. Less influential was heat addition in the injector tube. A variation of the SGS model or of the TVD limiter resulted in a moderate shift of the jet break-up. However, while SGS modeling appears to have no effect on the far field, the effect of changing the TVD limiter persists beyond jet break-up.

In addition to the results for transcritical injection, we now evaluate the results for supercritical conditions. Figure 9 compares the averaged density of experiment and simulation based on the case 4 of Mayer *et al.*⁴ As the injection temperature is here higher than the pseudo-boiling temperature, the injected nitrogen is in a supercritical state and the density is considerably smaller than for case 3. The density plateau that is observed in the measurements for the transcritical setup is shorter and the slope discontinuity in the fully turbulent region is extenuated. The figure includes LES results for ALDM with INCA (Case4-2) and results for the Vreman model obtained with INCA (Case4-3) as well as OpenFOAM (Case4-1). All simulations match the experimental data very well. ALDM and the two implementations of the Vreman model predict identical lengths of the potential core. However, both Vreman simulations under predict the density for $x/D > 20$, indicating that mixing is overpredicted. The ALDM result matches the measurements better and, with some reservations due to the noisy experimental data, its performance seems best overall.

C. Turbulence statistics

In order to further investigate the influence of real-gas thermodynamics on the jet dynamics, the axial and radial Reynolds stresses for case 3 and case 4 are analyzed close to the injector ($x/D \leq 10$). The results are averaged over $\Delta t \approx 0.18$ s and additionally in circumferential direction. To visualize their evolution at the shear layer between cold and warm nitrogen, we evaluate the maximum Reynolds-stress values in planes perpendicular to the flow direction as a function of the

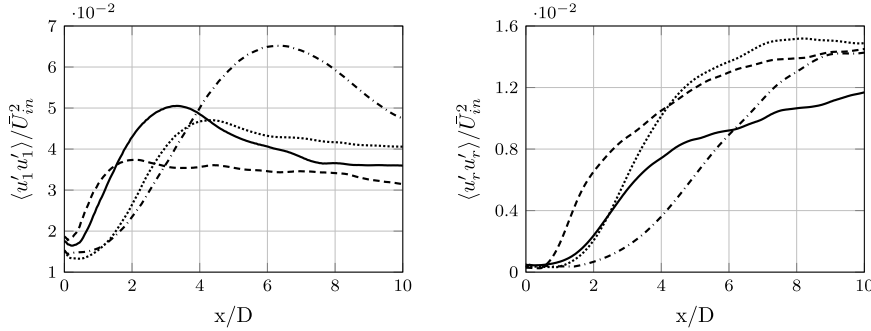


FIG. 10. Comparison of trans- and supercritical injections: Shown are axial profiles of maximum axial and radial Reynolds stresses as function of injector distance for explicit LES with Vreman model. — : Case3-1 (OpenFOAM), --- : Case3-5 (INCA), - - - : Case4-1 (OpenFOAM), ····· : Case4-3 (INCA).

injector distance. Additionally, we analyze the values of the axial and radial Reynolds stresses as a function of the radial distance from the centerline of the jet at four distinct positions of these planes. The radial position of the maximum values coincides with the position of the jet surface ($r/D = 0.5$ at the injector). Note that only the resolved Reynolds stress tensor is considered, the modeled SGS contribution is neglected.

Figure 10 shows the results for Case3-1 (OpenFOAM) and Case3-5 (INCA), in which nitrogen is injected in a transcritical state, and the results of the supercritical setups Case4-1 (OpenFOAM) and Case4-3 (INCA). In all cases, the radial fluctuations (right plot) show a section of zero growth immediately after injection, where the fluctuation amplitude is inferred by the boundary conditions, i.e., the incompressible pipe simulations presented in Sec. V B. Due to the coarser grid resolution, both INCA simulations start from a slightly lower resolved Reynolds stress level. In the supercritical cases, the growth starts earlier and the initial growth rate, i.e., the gradient in axial direction, is higher than in the transcritical cases. This effect is observed for both codes and is attributed to the density stratification effect, which is much stronger in Case3-1 and Case3-5. As mentioned earlier, Zong *et al.*^{10,11} argued that the density stratification transfers turbulence kinetic energy from the radial to the axial direction. Our LES confirms this argument.

While the growth of axial fluctuation fades at $x/D \approx 1.5$ for Case4-1, it continues until $x/D \approx 3$ for Case3-1. Despite quantitative differences, the same qualitative behavior is observed for the INCA simulations Case4-3 ($x/D \approx 3$) and Case3-5 ($x/D \approx 6$). The maximum axial fluctuations thus reach significantly higher values in the transcritical cases. For both simulations with INCA, the growth starts further downstream than for the simulations with OpenFOAM, which is caused by the difference in grid resolution, as the same inflow data are used for the particular INCA and OpenFOAM simulations. Because the grid for the OpenFOAM simulations is finer, it allows for a higher degree of resolved turbulence in the vicinity of the injector. This fact is more pronounced for the axial fluctuations than for the radial fluctuations, because the initial magnitude of the axial fluctuations (Reynolds stress anisotropy in wall boundary layers) is much higher. The values for the resolved maximal axial fluctuations grow in the shear layer between jet and ambient fluid and eventually reach higher values for the INCA simulations; this can be explained by the lower numerical dissipation of the INCA time integration scheme. These results are consistent for both the transcritical and the supercritical simulations.

Figure 11 shows radial profiles that further illustrate the findings. At $x/D = 2.5$, the axial and radial fluctuations show a narrow peak located at the jet surface. However, it is already visible that the peaks are broader for the supercritical cases Case4-1 and Case4-3, because of the lower density stratification. The radial fluctuations (right plot) clearly show the damping effect of the density gradient in Case3-1 and Case3-5 again. The plots at the locations further downstream show the development of the jet. Turbulence energy is transferred from the axial to the radial direction by the formation of Kelvin-Helmholtz type vortices, this is visible in the evolution of the maximum values of the axial and radial fluctuations. The shift of the peaks to higher values of r/D shows the

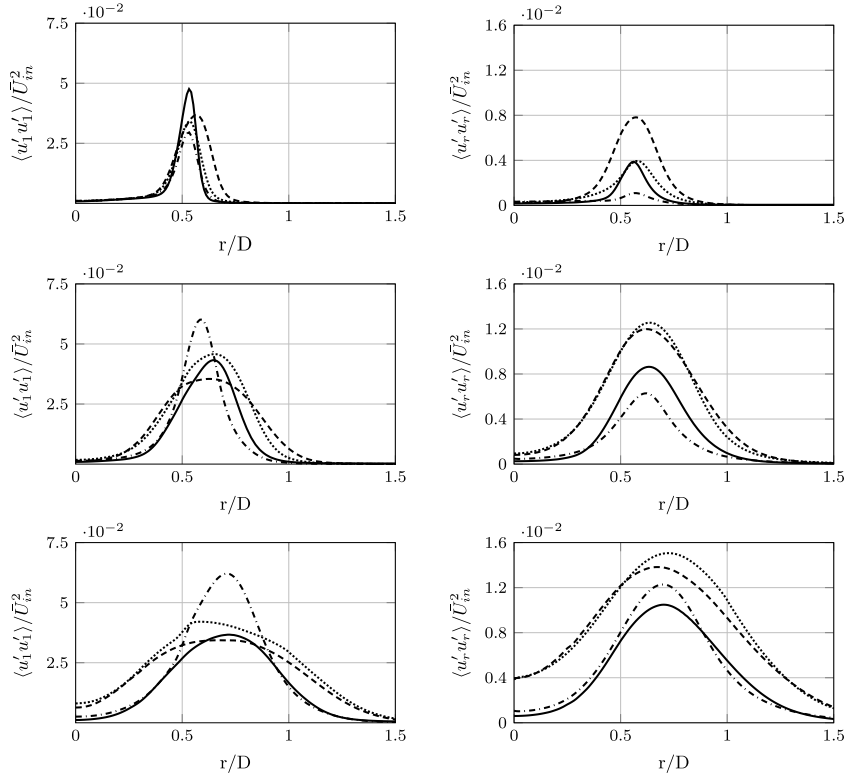


FIG. 11. Comparison of trans- and supercritical injections: Shown are radial profiles of axial and radial Reynolds stresses as function of the radial distance from the centerline at injector distances $x/D = 2.5, 5, 7.5$ (from top to bottom) for explicit LES with Vreman model. — : Case3-1 (OpenFOAM), --- : Case3-5 (INCA), - - - : Case4-1 (OpenFOAM), ····· : Case4-3 (INCA).

spreading of the jet, while the peaks themselves get smeared out because of the jet breaking up. This mechanism is delayed for Case3-1 and Case3-5, because the jet's dense core is stabilized by the high density stratification and a layer of high heat capacity as described in Sec. VI A. Finally, the plots for $x/D = 5$ and $x/D = 7.5$ give a hint why the location of jet break-up is the same for INCA and OpenFOAM with the Vreman model in the supercritical case, while in the transcritical case, the jet break-up happens further downstream with OpenFOAM than with INCA, cf. Figs. 8(d) and 9. The velocity fluctuations have a very similar profile for Case4-1 and Case4-3, whereas the magnitude and its growth rate is significantly lower in Case3-1 than for Case3-5, probably leading to the delayed break-up here.

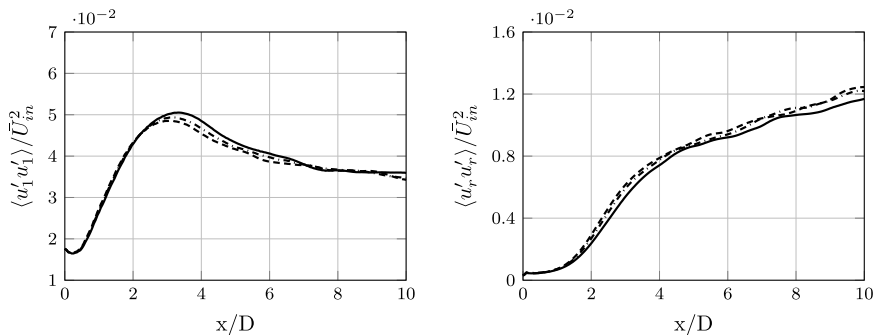


FIG. 12. Influence of volume translation: Shown are profiles of maximum axial and radial Reynolds stresses as function of injector distance. — : Case3-1 (PR-VTA EoS), --- : Case3-8 (PR EoS), - - - : Case3-9 (PR-VTH EoS).

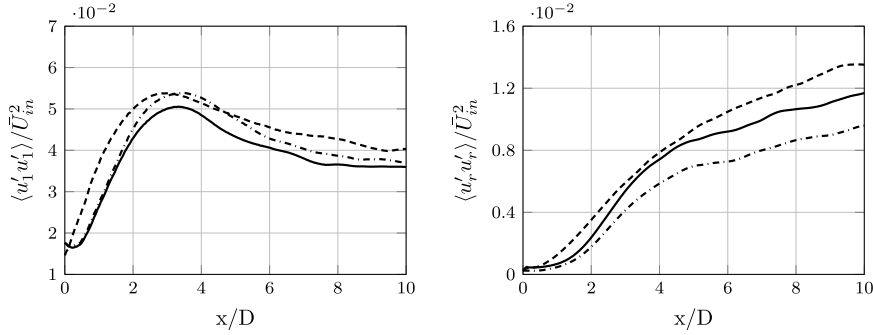


FIG. 13. Influence of the temperature inflow condition: Shown are profiles of maximum axial and radial Reynolds stresses as function of injector distance: — : Case3-1 (P-CD, $T_{in} = 128.53$ K), - - - : Case3-2 (P-CD, $T_{in} = 126.9$ K), - · - : Case3-3 (P-VD, $T_{in} = 128.53$ K).

A similar dependence of density stratification and turbulence as for the comparison of the trans- and supercritical cases can be observed in Fig. 12, where we compare the results for the transcritical case obtained from the simulations with different volume-translation methods. Results obtained with the PR-VTA EoS, which predicts the highest density, show the strongest damping of the surface-normal fluctuations and the highest amplification of the axial fluctuations. The two other EoSs follow in the order of their density predictions at the inlet.

Figure 13 demonstrates the effect of the different temperature inflow conditions. Comparing Case3-1 ($T_{in} = 128.53$ K) and Case3-2 ($T_{in} = 126.9$ K), it can be observed that decreasing the inlet temperature has a similar effect on the velocity fluctuations as changing the EoS. This is different in Case3-3, where heat addition in the injector is considered. Even though the turbulent intensity at the injector exit is smaller, see Fig. 4, the fluctuations increase rapidly and reach higher values than for Case3-1. This can be attributed to the washed out density gradient at the jet surface and the decreased damping effect associated with it.

In Fig. 14, results for simulations with different SGS models are compared. The resolved Reynolds stresses reveal that the differences between explicit and implicit LESs on the same grid are much stronger than one would assume from looking at the mean density profiles alone, cf. Fig. 8(c), where the difference, in particular between ALDM and Vreman, was rather small. This indicates that the location of jet break-up is essentially determined by the instability development on the large resolved scales, i.e., by the initial formation of Kelvin-Helmholtz vortices. The implicit LES with ALDM resolves more axial fluctuations right from the inflow than the explicit LES with eddy viscosity SGS models. The axial Reynolds stress then grows and reaches a maximum at $x/D \approx 4$, then decays slightly, and finally approaches a plateau for $x/D > 7$. The explicit LES, in

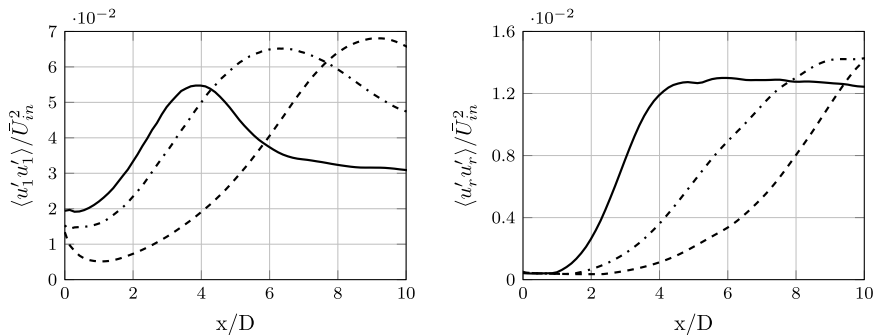


FIG. 14. Influence of the SGS modeling. Shown are profiles of maximum axial and radial Reynolds stresses as function of injector distance, which we obtained with INCA. — : Case3-4 (ALDM), - - - : Case3-5 (Vreman), - · - : Case3-6 (Smagorinsky).

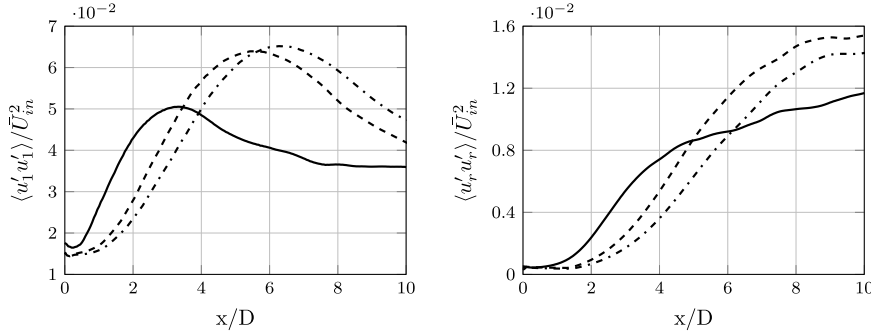


FIG. 15. Influence of the numerical method: Shown are profiles of maximum axial and radial Reynolds stresses as function of injector distance for explicit LES with Vreman model. — : Case3-1 (OpenFOAM: van Leer), - · - · : Case3-5 (INCA: van Leer), - - - : Case3-7 (INCA: Koren).

particular the Smagorinsky model, yields decaying fluctuation magnitudes during the early evolution. The transition to a fully turbulent mixing zone then starts from lower turbulence levels and evolves much slower than with ALDM. Peak values are reached at $x/D \approx 6$ with the Vreman model and at $x/D \approx 9$ with the Smagorinsky model. The strong damping of the axial fluctuation was also observed for the Smagorinsky model in OpenFOAM (not shown) and is clearly caused by an over estimation of the eddy viscosity in this region. Similar observations are made for the radial Reynolds stress, where ALDM predicts the maximum value at $x/D \approx 5$ and explicit SGS models at $x/D > 9$. This agrees with the jet break-up location inferred from the mean density profiles, which is shifted slightly downstream in the Smagorinsky results.

Finally, we compare maximum axial and radial Reynolds stresses for LES with identical turbulence model but different numerical methods, see Fig. 15. Results for Case3-5 (van Leer) and Case3-7 (Koren) show the effect of the TVD flux limiter and confirm our earlier argument that numerical dissipation delays the jet break-up by damping turbulence fluctuation. For both simulations with INCA, the initial growth starts later and the final amplitudes are higher than for the simulation with OpenFOAM (Case3-1). This is arguably caused by the coarser grid and the less dissipative time integration, which lead to a faster growth from an initially smaller amount of resolved turbulence. Interestingly, the Reynolds stress profiles obtained with OpenFOAM and Vreman model seem to more closely resemble the profiles for ALDM (Case3-4) than those for Case3-5, which is the INCA LES with Vreman model. This is another evidence of the sometime unpredictable effects caused by the interference between turbulence models and numerical methods.

VII. CONCLUDING REMARKS

The objective of this work was to contribute to a better understanding of the modeling requirements for predictive LES of cryogenic injection at supercritical pressures. LES of cryogenic injection is a very challenging task: On the one hand, the physical properties of the involved fluids vary strongly in the vicinity of the pseudo-critical temperature and thus a sophisticated but yet numerically efficient physical model is required to reproduce the correct behavior of the fluid. On the other hand, these strong variations require a robust computational method that is still able to capture the small-scale features of the turbulent flow without excessive numerical dissipation. We address these topics by a thorough analysis of the influence of the key parameters (turbulence inflow conditions, turbulence modeling, thermodynamic modeling, numerical dissipation, and grid resolution) on the numerical results obtained with two independently developed flow solvers, the density based INCA, and a pressure-based version of OpenFOAM, for the transcritical case 3 and the supercritical case 4 of the experimental database of Mayer *et al.*⁴

First, we found that the chosen inflow temperature plays a decisive role for the reproduction of the experimental results. Even small measurement uncertainties below 2 K lead to significant

changes in the liquid-like density of the injected fluid. We proposed to use the density measurements as a reference and to calculate a corrected inlet temperature based on a highly accurate equation of state. This approach gave much better results than directly matching the measured inlet temperature. We found that heat transfer from the injector wall to the fluid prior to injection has a strong effect on the turbulence intensity within the mixing zone and a notable but small effect on the overall jet flow evolution, in fact much less than was expected beforehand.

The choice of the thermodynamic modeling is again crucial for predicting the correct mean density evolution of the turbulent jet flow; however, it does not much affect the turbulence structures and the Reynolds stresses. The volume-translation method recently proposed by Abudour *et al.*²² gives superior results as compared to the uncorrected Peng-Robinson equation of state at little extra computational effort. It also outperforms the volume-translation method of Harstad *et al.*²¹ in terms of accuracy and computational efficiency.

We also found that the underlying SGS modeling plays a less important role if one is only interested in the mean flow. The mean density evolution for the supercritical case showed virtually no differences. Only small effects are observable for the transcritical case, where using the ALDM shifted the location of jet break-up upstream. This can be explained by the low-dissipative nature of ALDM, which allows for resolving more turbulence on the represented scales than the eddy-viscosity type models. A similar behavior could be observed when changing the flux limiter for the discretization of the inviscid fluxes in the explicit LES. Compared to the results of the simulation with van Leer's limiter,³⁹ the location of jet break-up shifted only slightly upstream when using the less diffusive Koren limiter.⁴⁰ However, both parameters, i.e., TVD limiter and SGS model, had a much larger than expected effect on the resolved Reynolds stress profiles. As the modeled SGS seems to have only minor impact on the mean density evolution, we conclude that the mechanism of jet break-up and mixing is mainly driven by the formation of large-scale Kelvin-Helmholtz vortices.

This conclusion is supported by the comparison of turbulence statistics for the transcritical case 3 and the supercritical case 4. In the transcritical case, a layer of high heat capacity encloses the jet core and the large density stratification damps the resolved radial fluctuations, transferring turbulence kinetic energy from the radial to the axial direction. This stabilizes the jet and leads to a longer dense core than in the supercritical case. These findings were consistent for all INCA and OpenFOAM results obtained with different numerical methods, different turbulence models, and on different grids. The mean flow results for the supercritical case 4 are also in good agreement with the experimental reference data. Therefore, we conclude that the physical and numerical models accurately represent the dynamically important flow features.

In summary, we observe that the relative influence of physical and numerical model uncertainties in the LES of injection at high pressures strongly depends on the thermodynamic regime that is investigated. If the injection condition is transcritical, the thermodynamics model is crucial for the prediction of first-order moments, whereas its effect is less strong at supercritical conditions. Given a sufficiently fine grid, the influence of SGS modeling and numerical flux discretization is essentially limited to second-order moments. For this reason, experimental data for higher-order statistics under controlled operating conditions would be highly appreciated. We found that moderate measurement uncertainties of the experimental operating conditions can hinder a conclusive comparison between simulation and measurements. Especially, the inflow temperature profile of the injected fluid is decisive and has a strong first-order effect on density and mass flow rate, for example. We acknowledge that precise temperature measurements are not easily obtained but they are crucially needed for the validation and verification of numerical tools at transcritical conditions.

ACKNOWLEDGMENTS

The authors gratefully acknowledge the German Research Foundation (Deutsche Forschungsgemeinschaft (DFG)) for providing financial support in the framework of SFB/TRR 40 *Fundamental Technologies for the Development of Future Space-Transport-System Components under*

High Thermal and Mechanical Loads and the Gauss Centre for Supercomputing e.V. (www.gauss-centre.eu) for funding this project by providing computing time on the GCS Supercomputer Super-MUC at Leibniz Supercomputing Centre (LRZ, <http://www.lrz.de>).

APPENDIX A: THERMODYNAMIC RELATIONS

The following shows the thermodynamic relations for various properties on the basis of the PR EoS.

1. Internal energy

An expression for the internal energy can be obtained using the departure function formalism (see Refs. 58 and 65)

$$(e - e^\circ) = \int_{\infty}^v \left[T \frac{\partial p}{\partial T} \Big|_v - p \right] dv, \quad (\text{A1})$$

where e is the molar internal energy and e° refers to its value at standard pressure, i.e., $p^\circ = 1$ bar. e° is evaluated with the 9-coefficient NASA polynomials⁵⁹ and v denotes the molar volume as obtained from the untranslated PR EoS ($v = v_{PR}$). The integral on the right side of Eq. (A1) represents the pressure dependent departure from the reference state and can be evaluated using the PR EoS

$$(e - e^\circ) = \frac{1}{2b\sqrt{2}} \left[a - T \frac{\partial a}{\partial T} \right] \ln \left[\frac{v + b(1 - \sqrt{2})}{v + b(1 + \sqrt{2})} \right], \quad (\text{A2})$$

where the coefficients a and b are defined in Sec. IV A.

2. Enthalpy

The enthalpy can be calculated analogously

$$\begin{aligned} (h - h^\circ) &= \int_{p^\circ}^p \left[v - T \frac{\partial v}{\partial T} \Big|_p \right] dp \\ &= pv - RT + \frac{1}{2b\sqrt{2}} \left[a - T \frac{\partial a}{\partial T} \right] \ln \left[\frac{v + b(1 - \sqrt{2})}{v + b(1 + \sqrt{2})} \right]. \end{aligned} \quad (\text{A3})$$

3. Heat capacity

The isobaric heat capacity follows directly from Eq. (A3),

$$\begin{aligned} c_p &= \frac{\partial h}{\partial T} \Big|_p \\ &= \frac{\partial h^\circ}{\partial T} \Big|_p - R - T \left[\frac{(\partial p / \partial T)_v^2}{(\partial p / \partial v)_T} - \frac{\partial^2 a}{\partial T^2} \frac{1}{2b\sqrt{2}} \ln \left[\frac{v + b(1 - \sqrt{2})}{v + b(1 + \sqrt{2})} \right] \right], \end{aligned} \quad (\text{A4})$$

with

$$\frac{\partial p}{\partial T} \Big|_v = \frac{R}{v - b} - \frac{\partial a / \partial T}{v^2 + 2vb - b^2}, \quad (\text{A5})$$

$$\frac{\partial p}{\partial v} \Big|_T = -\frac{RT}{(v - b)^2} + \frac{2a(v + b)}{(v^2 + 2vb - b^2)^2}. \quad (\text{A6})$$

The isochoric heat capacity can similarly be derived from Eq. (A1),

$$c_v = \left. \frac{\partial e}{\partial T} \right|_v = \left. \frac{\partial e^\circ}{\partial T} \right|_v - T \frac{\partial^2 a}{\partial T^2} \frac{1}{2b\sqrt{2}} \ln \left[\frac{v + b(1 - \sqrt{2})}{v + b(1 + \sqrt{2})} \right]. \quad (\text{A7})$$

4. Compressibility

The isothermal compressibility

$$\Psi_T = \left. \frac{\partial \rho}{\partial p} \right|_T = -\frac{1}{v^2} \left. \frac{\partial v}{\partial p} \right|_T \quad (\text{A8})$$

can be evaluated using Eq. (A6). However, with the real-gas adapted pressure-based solution algorithm presented in Sec. II B, the compressibility needs to be evaluated at isenthalpic conditions,

$$\Psi_h = \left. \frac{\partial \rho}{\partial p} \right|_h = -\frac{1}{v^2} \left. \frac{\partial v}{\partial p} \right|_h. \quad (\text{A9})$$

The partial derivative on the right side can be calculated using the mathematical relation

$$\left. \frac{\partial v}{\partial p} \right|_h = -\frac{(\partial h / \partial p)_v}{(\partial h / \partial v)_p}, \quad (\text{A10})$$

where

$$\begin{aligned} \left. \frac{\partial h}{\partial p} \right|_v &= v + \frac{(\partial h^\circ / \partial T)_p - R}{(\partial p / \partial T)_v} - \frac{T(\partial^2 a / \partial T^2)}{2b\sqrt{2}(\partial p / \partial T)_v} \ln \left[\frac{v + b(1 - \sqrt{2})}{v + b(1 + \sqrt{2})} \right], \\ \left. \frac{\partial h}{\partial v} \right|_p &= p + \frac{(\partial h^\circ / \partial T)_p - R}{(\partial v / \partial T)_p} + \frac{a - T(\partial a / \partial T)}{(v^2 + 2bv - b^2)^2} - \frac{T(\partial^2 a / \partial T^2)}{2b\sqrt{2}(\partial v / \partial T)_p} \ln \left[\frac{v + b(1 - \sqrt{2})}{v + b(1 + \sqrt{2})} \right], \end{aligned} \quad (\text{A11})$$

and

$$\left. \frac{\partial v}{\partial T} \right|_p = \frac{(\partial p / \partial T)_v}{(\partial p / \partial v)_T}. \quad (\text{A12})$$

A comparison between the two formulations is shown in Fig. 1.

5. Speed of sound

The speed of sound is evaluated in order to determine the appropriate time step in the density based INCA,

$$a_s = v \sqrt{\left. \frac{c_p}{c_v} \frac{\partial p}{\partial v} \right|_T}. \quad (\text{A13})$$

APPENDIX B: TRANSPORT MODEL OF CHUNG *et al.*⁶⁰

1. Dynamic viscosity

The viscosity is calculated as follows:

$$\mu = \mu^* \frac{36.344(MT_c)^{1/2}}{v_c^{2/3}}, \quad (\text{B1})$$

where

$$\begin{aligned}
 M &= \text{molecular weight in [g/mol]}, \\
 \mu^* &= \frac{(T^*)^{1/2}}{\Omega_v} (F_c [(G_2)^{-1} + E_6 y]) + \mu^{**}, \\
 T^* &= 1.2593 T/T_c, \\
 F_c &= 1 - 0.2756 \omega, \\
 \Omega_v &= [A(T^*)^{-B}] + C[\exp(-DT^*)] + E[\exp(-FT^*)], \\
 y &= \frac{\rho v_c}{6}, \\
 G_1 &= \frac{1 - 0.5y}{(1 - y)^3}, \\
 G_2 &= \frac{E_1 ([1 - \exp(-E_4 y)]/y) + E_2 G_1 \exp(E_5 y) + E_3 G_1}{E_1 E_4 + E_2 + E_3}, \\
 \mu^{**} &= E_7 y^2 G_2 \exp[E_8 + E_9 (T^*)^{-1} + E_{10} (T^*)^{-2}].
 \end{aligned}$$

The parameters E_1 to E_{10} as well as the constants A to F can be found in the original publication of Chung *et al.*⁶⁰

2. Thermal conductivity

The thermal conductivity is calculated as follows:

$$\lambda = \frac{36.2\mu^0\Psi}{M'}(G_3^{-1} + B_6 y) + qB_7 y^2 T_r^{1/2} G_3, \quad (\text{B2})$$

where

$$\begin{aligned}
 \mu^0 &= \frac{26.69F_c(MT)^{0.5}}{\sigma^2\Omega_v}, \\
 M' &= \text{molecular weight in (kg/mol)}, \\
 \sigma &= 0.809 v_c^{1/3}, \\
 \Psi &= 1 + \alpha ([0.215 + 0.28288\alpha - 1.061\beta + 0.26665Z]/[0.6366 + \beta Z + 1.061\alpha\beta]), \\
 \alpha &= C_v/R - 3/2, \\
 \beta &= 0.7862 - 0.7109\omega + 1.3168\omega^2, \\
 Z &= 2.0 + 10.5T_r^2, \\
 q &= 3.586 \cdot 10^{-3} (T_c/M')^{1/2} / V_c^{2/3}, \\
 G_3 &= \frac{(B_1/y)[1 - \exp(-B_4 y)] + B_2 G_1 \exp(B_5 y) + B_3 G_1}{B_1 B_4 + B_2 + B_3}.
 \end{aligned}$$

The parameters B_1 to B_{10} are provided as linear functions of ω and can be found in the original publication of Chung *et al.*⁶⁰

¹ E. Messerschmid and S. Fasoulas, *Raumfahrtssysteme*, 3rd ed. (Springer, 2009), ISBN: 978-3-540-77699-4.

² M. Oschwald, J. J. Smith, R. Branam, J. Hussong, and A. Schik, "Injection of fluids into supercritical environments," *Combust. Sci. Technol.* **178**(1-3), 49–100 (2006).

³ B. Chehroudi, "Recent experimental efforts on high-pressure supercritical injection for liquid rockets and their implications," *Int. J. Aerosp. Eng.* **2012**, 121802 (2012).

⁴ W. Mayer, J. Telaar, R. Branam, G. Schneider, and J. Hussong, "Raman measurements of cryogenic injection at supercritical pressure," *Heat Mass Transfer* **39**(8-9), 709–719 (2003).

⁵ J. Telaar, G. Schneider, J. Hussong, and W. Mayer, "Cryogenic jet injection: Test case RCM 1," in *Proceedings of the 2nd International Workshop on Rocket Combustion Modeling* (Elsevier, Amsterdam, The Netherlands, 2001), pp. 25–27.

⁶ B. Chehroudi, R. Cohn, D. Talley, and A. Badakhshan, "Raman scattering measurement in the initial region of sub- and supercritical jets," AIAA Paper No. 2000-3392, 2000.

⁷ M. Oschwald and A. Schik, "Supercritical nitrogen free jet investigated by spontaneous Raman scattering," *Exp. Fluids* **27**(6), 497–506 (1999).

⁸ W. Mayer and H. Tamura, "Propellant injection in a liquid oxygen/gaseous hydrogen rocket engine," *J. Propul. Power* **12**, 1137–1147 (1996).

- ⁹ J. C. Oefelein and V. Yang, "Modeling high-pressure mixing and combustion processes in liquid rocket engines," *J. Propul. Power* **14**(5), 843–857 (1998).
- ¹⁰ N. Zong, H. Meng, S.-Y. Hsieh, and V. Yang, "A numerical study of cryogenic fluid injection and mixing under supercritical conditions," *Phys. Fluids* **16**(12), 4248–4261 (2004).
- ¹¹ N. Zong and V. Yang, "Cryogenic fluid jets and mixing layers in transcritical and supercritical environments," *Combust. Sci. Technol.* **178**(1-3), 193–227 (2006).
- ¹² J. C. Oefelein, "Mixing and combustion of cryogenic oxygen-hydrogen shear-coaxial jet flames at supercritical pressure," *Combust. Sci. Technol.* **178**(1-3), 229–252 (2006).
- ¹³ T. Schmitt, L. Selle, B. Cuenot, and T. Poinot, "Large-eddy simulation of transcritical flows," *C. R. Mec.* **337**(6), 528–538 (2009).
- ¹⁴ D.-Y. Peng and D. P. Robinson, "A new two-constant equation of state," *Ind. Eng. Chem. Fundam.* **15**(1), 59–64 (1976).
- ¹⁵ T. Kim, Y. Kim, and S.-K. Kim, "Numerical study of cryogenic liquid nitrogen jets at supercritical pressures," *J. Supercrit. Fluids* **56**(2), 152–163 (2011).
- ¹⁶ G. Soave, "Equilibrium constants from a modified Redlich-Kwong equation of state," *Chem. Eng. Sci.* **27**(6), 1197–1203 (1972).
- ¹⁷ *NIST Chemistry WebBook*, edited by P. J. Linstrom and W. G. Mallard, NIST Standard Reference Database Number 69 (NIST, National Institute of Standards and Technology, 2011), URL: <http://webbook.nist.gov/chemistry/fluid/>.
- ¹⁸ A. Urbano and F. Nasuti, "Conditions for the occurrence of heat transfer deterioration in light hydrocarbons flows," *Heat Mass Transfer* **65**, 599–609 (2013).
- ¹⁹ O. Kunz, R. Klimeck, W. Wagner, and M. Jaeschke, *The GERG-2004 Wide-Range Equation of State for Natural Gases and Other Mixtures* (VDI, Düsseldorf, 2007).
- ²⁰ J. Matheis, H. Müller, C. Lenz, M. Pfitzner, and S. Hickel, "Volume translation methods for real-gas computational fluid dynamics simulations," *J. Supercrit. Fluids* **107**, 422–432 (2016).
- ²¹ K. G. Harstad, R. S. Miller, and J. Bellan, "Efficient high-pressure state equations," *AIChE J.* **43**(6), 1605–1610 (1997).
- ²² A. M. Abudour, S. A. Mohammad, R. L. Robinson, Jr., and K. A. M. Gasem, "Volume-translated Peng–Robinson equation of state for saturated and single-phase liquid densities," *Fluid Phase Equilib.* **335**, 74–87 (2012).
- ²³ M. Jarczyk and M. Pfitzner, "Large eddy simulation of supercritical nitrogen jets," AIAA Paper No. 2012-1270, 2012.
- ²⁴ C. A. Niedermeier, H. Müller, M. Jarczyk, S. Hickel, N. A. Adams, and M. Pfitzner, "Large-eddy simulation of turbulent trans- and supercritical mixing," AIAA Paper No. 2013-2950, 2013.
- ²⁵ L. C. Selle, N. A. Okong'o, J. Bellan, and K. G. Harstad, "Modelling of subgrid-scale phenomena in supercritical transitional mixing layers: An *a priori* study," *J. Fluid Mech.* **593**, 57–91 (2007).
- ²⁶ T. S. Park, "LES and RANS simulations of cryogenic liquid nitrogen jets," *J. Supercrit. Fluids* **72**, 232–247 (2012).
- ²⁷ X. Petit, G. Ribert, G. Lartigue, and P. Domingo, "Large eddy simulation of supercritical fluid injection," *J. Supercrit. Fluids* **84**, 61–73 (2013).
- ²⁸ A. W. Vreman, "An eddy-viscosity subgrid-scale model for turbulent shear flow: Algebraic theory and applications," *Phys. Fluids* **16**(10), 3670–3681 (2004).
- ²⁹ J. Smagorinsky, "General circulation experiments with the primitive equations. I. The basic experiment," *Mon. Weather Rev.* **91**(3), 99–164 (1963).
- ³⁰ S. Hickel, N. A. Adams, and J. A. Domaradzki, "An adaptive local deconvolution method for implicit LES," *J. Comput. Phys.* **213**(1), 413–436 (2006).
- ³¹ S. Hickel, C. P. Egerer, and J. Larsson, "Subgrid-scale modeling for implicit large eddy simulation of compressible flows and shock-turbulence interaction," *Phys. Fluids* **26**, 106101 (2014).
- ³² M. Klein, A. Sadiki, and J. Janicka, "A digital filter based generation of inflow data for spatially developing direct numerical or large eddy simulations," *J. Comput. Phys.* **186**(2), 652–665 (2003).
- ³³ T. Schmitt, J. Rodriguez, I. A. Leyva, and S. Candel, "Experiments and numerical simulation of mixing under supercritical conditions," *Phys. Fluids* **24**(5), 055104 (2012).
- ³⁴ H. Müller, J. Matheis, M. Pfitzner, and S. Hickel, "Large-eddy simulation of coaxial LN₂/GH₂ injection at trans- and supercritical conditions," *J. Propul. Power* (published online 2015).
- ³⁵ D. T. Banuti and K. Hannemann, "Effect of injector wall heat flux on cryogenic injection," AIAA Paper No. 2010-7139, 2010.
- ³⁶ M. Meyer, A. Devesa, S. Hickel, X. Y. Hu, and N. A. Adams, "A conservative immersed interface method for large-eddy simulation of incompressible flows," *J. Comput. Phys.* **229**(18), 6300–6317 (2010).
- ³⁷ F. Örley, V. Pasquariello, S. Hickel, and N. A. Adams, "Cut-element based immersed boundary method for moving geometries in compressible liquid flows with cavitation," *J. Comput. Phys.* **283**, 1–22 (2015).
- ³⁸ S. Gottlieb and C. W. Shu, "Total variation diminishing Runge–Kutta schemes," *Math. Comput.* **67**(221), 73–85 (1998).
- ³⁹ B. van Leer, "Towards the ultimate conservative difference scheme. II. Monotonicity and conservation combined in a second-order scheme," *J. Comput. Phys.* **14**(4), 361–370 (1974).
- ⁴⁰ B. Koren, "A robust upwind discretization method for advection, diffusion and source terms," in *Numerical Methods for Advection-Diffusion Problems*, edited by C. B. Vreugdenhil and B. Koren (Vieweg, Braunschweig, 1993), pp. 117–138.
- ⁴¹ P. L. Roe, "Characteristic-based schemes for the Euler equations," *Annu. Rev. Fluid Mech.* **18**, 337–365 (1986).
- ⁴² E. S. Taskinoglu and J. Bellan, "A posteriori study using a DNS database describing fluid disintegration and binary-species mixing under supercritical pressure: Heptane and nitrogen," *J. Fluid Mech.* **645**, 211–254 (2010).
- ⁴³ E. S. Taskinoglu and J. Bellan, "Subgrid-scale models and large-eddy simulation of oxygen stream disintegration and mixing with a hydrogen or helium stream at supercritical pressure," *J. Fluid Mech.* **679**, 156–193 (2011).
- ⁴⁴ R. Issa, "Solution of the implicitly discretised fluid flow equations by operator-splitting," *J. Comput. Phys.* **62**(1), 40–65 (1985).
- ⁴⁵ R. Issa, B. Ahmadi-Befrui, K. Beshay, and A. Grosman, "Solution of the implicitly discretised reacting flow equations by operator splitting," *J. Comput. Phys.* **93**(2), 388–410 (1991).

- ⁴⁶ M. Jarczyk, "Numerische modellierung von turbulenten Strömungen realer gasgemische," Ph.D. thesis, Universität der Bundeswehr München, 2013.
- ⁴⁷ V. Pasquariello, M. Grilli, S. Hickel, and N. A. Adams, "Large-eddy simulation of passive shock-wave/boundary-layer interaction control," *Int. J. Heat Fluid Flow* **49**, 116–127 (2014).
- ⁴⁸ M. Grilli, S. Hickel, and N. A. Adams, "Large-eddy simulation of a supersonic turbulent boundary layer over a compression–expansion ramp," *Int. J. Heat Fluid Flow* **42**, 79–93 (2013).
- ⁴⁹ J. F. Quaatz, M. Giglmaier, S. Hickel, and N. A. Adams, "Large-eddy simulation of a pseudo-shock system in a laval nozzle," *Int. J. Heat Fluid Flow* **49**, 108–115 (2014).
- ⁵⁰ C. P. Egerer, S. Hickel, S. J. Schmidt, and N. A. Adams, "Large-eddy simulation of turbulent cavitating flow in a micro channel," *Phys. Fluids* **26**(8), 085102 (2014).
- ⁵¹ F. Orley, T. Trummel, S. Hickel, M. S. Mihatsch, S. J. Schmidt, and N. A. Adams, "Large-eddy simulation of cavitating nozzle flow and primary jet break-up," *Phys. Fluids* **27**(8), 086101 (2015).
- ⁵² D. J. Hill and D. I. Pullin, "Hybrid tuned center-difference-WENO method for large eddy simulations in the presence of strong shocks," *J. Comput. Phys.* **194**(2), 435–450 (2004).
- ⁵³ X. Y. Hu, N. A. Adams, and C.-W. Shu, "Positivity-preserving method for high-order conservative schemes solving compressible Euler equations," *J. Comput. Phys.* **242**, 169–180 (2013).
- ⁵⁴ S. Remmler and S. Hickel, "Spectral eddy viscosity of stratified turbulence," *J. Fluid Mech.* **755**, R6 (2014).
- ⁵⁵ R. A. Clark, J. H. Ferziger, and W. C. Reynolds, "Evaluation of subgrid-scale models using an accurately simulated turbulent flow," *J. Fluid Mech.* **91**(1), 1–16 (1979).
- ⁵⁶ G. Erlebacher, M. Y. Hussaini, C. G. Speziale, and T. A. Zang, "Towards the large-eddy simulation of compressible turbulent flows," *J. Fluid Mech.* **238**, 155–185 (1992).
- ⁵⁷ C. Fureby, "On subgrid scale modeling in large eddy simulations of compressible fluid flow," *Phys. Fluids* **8**(5), 1301–1311 (1996).
- ⁵⁸ B. E. Poling, J. M. Prausnitz, and J. P. O'Connell, *The Properties of Gases and Liquids*, 5th ed. (Mcgraw-Hill Professional, 2000).
- ⁵⁹ E. Goos, A. Burcat, and B. Ruscic, "Extended third millennium ideal gas and condensed phase thermochemical database for combustion with updates from active thermochemical tables," Report No. TAE 960, Technion –Israel Institute of Technology, Haifa, 2009, URL: <http://burcat.technion.ac.il/dir>.
- ⁶⁰ T.-H. Chung, M. Ajlan, L. L. Lee, and K. E. Starling, "Generalized multiparameter correlation for nonpolar and polar fluid transport properties," *Ind. Eng. Chem. Res.* **27**(4), 671–679 (1988).
- ⁶¹ J. M. Prausnitz, R. N. Lichtenthaler, and E. G. de Azevedo, *Molecular Thermodynamics of Fluid-phase Equilibria*, 2nd ed. (Prentice Hall, 1986).
- ⁶² J. J. Martin, "Cubic equations of state - which?," *Ind. Eng. Chem. Fundam.* **18**(2), 81–97 (1979).
- ⁶³ G. F. Chou and J. M. Prausnitz, "A phenomenological correction to an equation of state for the critical region," *AIChE J.* **35**(9), 1487–1496 (1989).
- ⁶⁴ R. Span, E. W. Lemmon, R. T. Jacobsen, W. Wagner, and A. Yokozeki, "A reference equation of state for the thermodynamic properties of nitrogen for temperatures from 63.151 to 1000 K and pressures to 2200 MPa," *J. Phys. Chem. Ref. Data* **29**(6), 1361–1433 (2000).
- ⁶⁵ J. R. Elliott and C. T. Lira, *Introductory Chemical Engineering Thermodynamics*, 2nd ed. (Prentice Hill, 2012).